

Density functional approach to elastic properties of three-dimensional dipole-spring models for magnetic gels

Cite as: J. Chem. Phys. **158**, 054909 (2023); <https://doi.org/10.1063/5.0133207>

Submitted: 02 November 2022 • Accepted: 16 January 2023 • Accepted Manuscript Online: 17 January 2023 • Published Online: 06 February 2023

 Segun Goh,  Andreas M. Menzel,  René Wittmann, et al.



View Online



Export Citation



CrossMark

ARTICLES YOU MAY BE INTERESTED IN

[Inhomogeneous steady shear dynamics of a three-body colloidal gel former](#)

The Journal of Chemical Physics **158**, 054908 (2023); <https://doi.org/10.1063/5.0130655>

[Large amplitude oscillatory shear study of a colloidal gel near the critical state](#)

The Journal of Chemical Physics **158**, 054907 (2023); <https://doi.org/10.1063/5.0129416>

[The network structure of the corneal endothelium](#)

The Journal of Chemical Physics **158**, 055101 (2023); <https://doi.org/10.1063/5.0134667>



Time to get excited.
Lock-in Amplifiers – from DC to 8.5 GHz

[Find out more](#)

 Zurich
Instruments

Density functional approach to elastic properties of three-dimensional dipole-spring models for magnetic gels

Cite as: J. Chem. Phys. 158, 054909 (2023); doi: 10.1063/5.0133207

Submitted: 2 November 2022 • Accepted: 16 January 2023 •

Published Online: 6 February 2023



View Online



Export Citation



CrossMark

Segun Goh,^{1,2,a)}  Andreas M. Menzel,^{3,b)}  René Wittmann,^{2,c)}  and Hartmut Löwen^{2,d)} 

AFFILIATIONS

¹Theoretical Physics of Living Matter, Institute of Biological Information Processing, Forschungszentrum Jülich, 52425 Jülich, Germany

²Institut für Theoretische Physik II: Weiche Materie, Heinrich-Heine-Universität Düsseldorf, Universitätsstr. 1, 40225 Düsseldorf, Germany

³Institut für Physik, Otto-von-Guericke-Universität Magdeburg, Universitätsplatz 2, 39106 Magdeburg, Germany

^{a)} Author to whom correspondence should be addressed: s.goh@fz-juelich.de

^{b)} Electronic mail: a.menzel@ovgu.de

^{c)} Electronic mail: rene.wittmann@hhu.de

^{d)} Electronic mail: hlowen@hhu.de

ABSTRACT

Magnetic gels are composite materials consisting of a polymer matrix and embedded magnetic particles. Those are mechanically coupled to each other, giving rise to the magnetostrictive effects as well as to a controllable overall elasticity responsive to external magnetic fields. Due to their inherent composite and thereby multiscale nature, a theoretical framework bridging different levels of description is indispensable for understanding the magnetomechanical properties of magnetic gels. In this study, we extend a recently developed density functional approach from two spatial dimensions to more realistic three-dimensional systems. Along these lines, we connect a mesoscopic characterization resolving the discrete structure of the magnetic particles to macroscopic continuum parameters of magnetic gels. In particular, we incorporate the long-range nature of the magnetic dipole–dipole interaction and consider the approximate incompressibility of the embedding media and relative rotations with respect to an external magnetic field breaking rotational symmetry. We then probe the shape of the model system in its reference state, confirming the dependence of magnetostrictive effects on the configuration of the magnetic particles and on the shape of the considered sample. Moreover, calculating the elastic and rotational coefficients on the basis of our mesoscopic approach, we examine how the macroscopic types of behavior are related to the mesoscopic properties. Implications for real systems of random particle configurations are also discussed.

Published under an exclusive license by AIP Publishing. <https://doi.org/10.1063/5.0133207>

I. INTRODUCTION

Ferrogels, magnetic gels, as well as magnetorheological gels and elastomers, all referred to as magnetic gels, are soft elastic composite materials containing magnetic or magnetizable particles, both simply referred to as magnetic particles. Their mechanical properties are controllable by external magnetic fields.^{1–4} The composite nature arises as the magnetic particles are mechanically coupled to a surrounding polymeric matrix.^{5–9} Such a magnetomechanical coupling has even been enhanced by anchoring polymers directly on the surface of magnetic particles.^{2,5,6,9} To understand the rheological

properties of these materials, the dependence of their elastic moduli and magnetostrictive effects on external magnetic fields has been investigated in various settings.^{10–17} In particular, induced changes in the configuration of the magnetic particles, especially the touching of adjacent particles and chain formation, have been repeatedly reported as prominent features in the response of magnetic gels to external magnetic fields.^{7,18–23}

Due to their inherent composite nature, a complete theoretical understanding of magnetic gels is still challenging.²⁴ At macroscopic scales, thermodynamic and hydrodynamic theories have been developed,^{25–27} in which both the magnetic and elastic components

are modeled as homogeneous continua. Notably, the positive magnetostriction, namely, elongation along the magnetic field direction, has been predicted using such continuum approaches.^{28–30} However, potential effects stemming from the detailed configurations of the magnetic particles and the polymers as well as the mechanisms governing these effects are hardly resolved at this scale. Rather, phenomenological coefficients have to be determined via modeling or experiments. In a theoretical perspective, one may consider a model resolving all the magnetic particles and polymer molecules at a microscopic level. Indeed, numerical simulation studies have been performed at this scale, revealing the roles of the polymer network topology and the coupling between the orientation of magnetic particles and the surrounding polymers,^{31,32} as well as the degree of cross-linking in the polymer matrix.³³ However, unifying all the ingredients of such models to derive macroscopic parameters remains a demanding task.

In this regard, mesoscopic approaches still address the configurations of the magnetic particles explicitly, while individual polymeric building blocks are not resolved. Indeed, the significance of detailed structures at mesoscopic length scales has been revealed, as the mesoscopic models predict, for instance, both positive and negative magnetostrictive effects depending on the specific configuration of the magnetic particles.^{34–37} The rotational fluctuations of magnetic particles have also been addressed within a mesoscopic approach.³⁸ Specifically, the polymer matrix can be coarse-grained as an elastic continuum.^{39–42} We note that the role of the magnetic particles can also be modeled using continuum fields^{43,44} that describe the particle arrangements.

Alternatively, the elastic continuum can be discretized on the mesoscopic scale as a network of harmonic springs.^{45–47} One advantage of this approach is that microscopic theories as well as simulation techniques developed in the framework of statistical mechanics are directly applicable. The interaction energies are explicitly defined in this case. As demonstrated in Ref. 48 using a description of a uniaxial magnetic gel, and in Refs. 24 and 49 using an approach for isotropic one- and two-dimensional systems, a bridging description between mesoscopic and macroscopic scales may unravel the role of the discrete mesoscopic structures in the materials for the macroscopic behavior. In this way, the gap between continuum theories and mesoscopic models is closed.

In the present study, we further explore the issue of scale-bridging and, in particular, the statistical mechanics of magnetic gels. As for the mesoscopic description, we employ a simple but tangible model consisting of magnetic dipolar particles and harmonic springs connecting them. Starting from the mesoscale model, we aim at calculating macroscopic elastic and rotational coefficients, the trend of which we then correlate with mesoscopic characteristics, i.e., the configuration of the magnetic particles. Specifically, we employ classical density functional theory (DFT),^{50–53} extending the concept of mapping the elastic interactions between the particles through the surrounding elastic medium onto pseudospings^{24,49} to three dimensions. The resulting free energy allows for a calculation of macroscopic elasticity parameters.

To this end, the following issues need to be addressed in advance. First, the dipolar magnetic interaction is strictly long-ranged, rendering the system thermodynamically ill-defined.⁵⁴ While the Ewald summation technique^{55,56} can be adopted to numerically simulate systems with long-range interactions, such as

suspensions of magnetic particles in liquid crystalline matrices,^{57,58} the shape dependence of the free energy has to be clarified as in the studies of dipolar fluids^{59,60} and of magneto-sensitive elastomers.⁶¹ In addition, we note that the aforementioned magnetostrictive effects originate from the anisotropic nature of the magnetic dipole–dipole interaction. These points require a careful choice of the DFT implementation. Second, thermal fluctuations of the magnetic particles need to be included. As we develop a statistical theory for the equilibrium free energy, i.e., DFT, this issue is resolved automatically. Third, when an external magnetic field explicitly breaks the rotational symmetry of the system, relative rotations with respect to the field direction should be considered in the underlying elasticity theory. In this case, elastic materials are no longer invariant under rotations, and, therefore, a rotation is accompanied by a corresponding energy cost. Equivalently to elastic moduli quantifying the resistance to stresses, rotation coefficients are used to characterize to which extent a material resists to torques. Originally, this concept was introduced in the context of liquid-crystalline elastomers^{62–65} but has also been extended to uniaxial magnetic gels.^{26,48} Finally, the role of incompressibility that may be inherent in many systems of magnetic gels should also be clarified in the description. Just as conventional gels, magnetic gels can swell/shrink by absorbing/releasing liquid. Otherwise, they are regarded as incompressible, for instance, due to the dispersed fluid. Such incompressibility may alter the mechanical properties of magnetic gels,^{15,66} calling for a theory respecting volume conservation.

This paper is organized as follows: In Sec. II, our model for magnetic gels is introduced. The DFT for our model system and its implementation are described in Sec. III. In Sec. IV, we investigate the elastic and rotation coefficients as well as magnetostrictive effects from the DFT calculation based on a nonlinear framework for elasticity under constraints. Finally, discussions are included in Sec. V. Technical details are shifted to the appendices.

II. MESOSCOPIC DIPOLE-SPRING MODEL

We consider a three-dimensional version of the previously studied dipole-spring system^{46,67} as a mesoscopic model for magnetic gels. The model consists of N identical magnetic particles of diameter σ_D and dipole moment \mathbf{m} , which are connected by identical harmonic springs of spring constant k_{el} and rest length a_{el} . We denote the position of the i th particle by \mathbf{r}_i ($i = 1, \dots, N$).

The total Hamiltonian \mathcal{H}_{tot} of the system is introduced as the sum of the kinetic part \mathcal{H}_{kin} and the interaction part \mathcal{H}_{int} of the magnetic particles, the latter of which splits into three parts,

$$\mathcal{H}_{int} = \mathcal{H}_m + \mathcal{H}_{el} + \mathcal{H}_{st}. \quad (1)$$

Here, \mathcal{H}_m and \mathcal{H}_{st} , respectively, denote the energies of the magnetic dipole–dipole interaction and the steric repulsion, which are all-to-all pairwise additive. Therefore, with $\mathbf{r}_{ij} = \mathbf{r}_j - \mathbf{r}_i$, they take the form

$$\mathcal{H}_{m,st} = \frac{1}{2} \sum_{i \neq j} u_{m,st}(\mathbf{r}_{ij}), \quad (2)$$

where u_m and u_{st} denote the two-body magnetic dipole–dipole interaction and steric repulsion, respectively, as detailed below.

In stark contrast to Eq. (2), the elastic part \mathcal{H}_{el} does not simply take the form of a pairwise additive potential, namely, no general two-body potential applying simultaneously to all pairs of particles can be introduced. Specifically, the elastic contribution is written in the form

$$\mathcal{H}_{\text{el}} = \sum_{\langle ij \rangle} u_{\text{el}}(r_{ij}) = \sum_{\langle ij \rangle} \frac{1}{2} k_{\text{el}} (r_{ij} - a_{\text{el}})^2, \quad (3)$$

where $\langle i, j \rangle$ indicates that the sum only includes a predefined set of neighbors, which labels the particles such that they become distinguishable. Thus, the potential energy cannot be written as a sum over pair potentials of indistinguishable particles. For the two-body potential u_{el} , a harmonic spring potential of spring constant k_{el} is adopted, while a_{el} is the rest length of the springs and $r_{ij} = |\mathbf{r}_{ij}|$. Here, we assume a face-centered cubic (FCC) lattice structure with twelve nearest-neighbor particles, which is indicated by the angular bracket in Eq. (3). Therefore, in total, $6N$ harmonic springs connect the nearest-neighboring pairs of magnetic particles in this specific model (except for boundary effects).

Next, for the two-body steric repulsion in Eq. (2), we assume a particle diameter σ_D and adopt a hard-core potential in the form of

$$u_{\text{st}}(\mathbf{r}) = \begin{cases} 0 & \text{if } r \geq \sigma_D, \\ \infty & \text{otherwise.} \end{cases} \quad (4)$$

As a dimensionless density, we introduce the packing fraction η defined as the fraction of the volume occupied by the magnetic particles, i.e., $\eta \equiv N(4\pi/3)(\sigma_D/2)^3/V$, where V is the volume of the system.

Specifying the two-body magnetic dipole–dipole interaction energy, the two-body potential in Eq. (2) reads

$$u_m(\mathbf{r}) = \frac{\mu_0}{4\pi} \left[\frac{\mathbf{m} \cdot \mathbf{m}}{r^3} - \frac{3(\mathbf{m} \cdot \mathbf{r})(\mathbf{m} \cdot \mathbf{r})}{r^5} \right], \quad (5)$$

where μ_0 is the vacuum permeability. The magnetic moment \mathbf{m} is determined by the applied magnetic field $\mathbf{H} = H\hat{z}$, which is always directed along the z -direction, and the magnetization properties of each magnetic particle (see, e.g., Refs. 68 and 69). When an external magnetic field is applied, we assume that $\mathbf{m}(\mathbf{H}) \parallel \mathbf{H}$, i.e., $\mathbf{m} = m\hat{z}$ [see Fig. 1(a) for illustration]. In the absence of the applied field, magnetic particles may or may not retain their magnetization. Here, we consider two simple cases. First, in Model I, we assume that the magnetic particles are ferromagnetic. There, the magnetic moment of each particle persists and is fixed with respect to the orientation of the material body (the FCC lattice in this study), once the magnetic particles are magnetized. We then investigate elastic properties of the model system in the absence of external fields as depicted in Fig. 1(b). In this case, the dipole moment \mathbf{m} rotates rigidly with the whole system. In Model II, we assume that the magnetic particles are paramagnetic. To retain the magnetization, the external field \mathbf{H} needs to be persistently applied to the system in this case. In contrast to Model I, \mathbf{m} is then always directed along \mathbf{H} as shown in Fig. 1(c), even when the whole system rotates. Consequently, relative rotations between the magnetization direction and the rest of the system become relevant. We note that the magnetic dipole–dipole interaction breaks the isotropy of the system both in Model I and Model II.

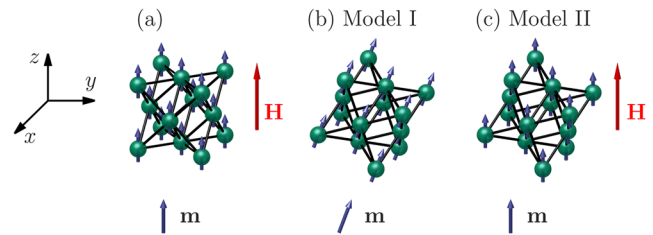


FIG. 1. Illustration of the model. Cubic unit cells of the face-centered cubic lattice consisting of magnetic particles (green spheres) are shown. Black solid lines represent springs connecting the magnetic particles, and blue arrows indicate the dipole moments \mathbf{m} of the particles. (a) Under an external magnetic field \mathbf{H} , the magnetic dipole moments are aligned along the external field direction \mathbf{H} (red arrow) in the initial state. Regarding rotations, we consider two models: (b) Model I for idealized ferromagnetic particles and (c) Model II for idealized paramagnetic particles. As the dipole moments of ferromagnetic particles persist even under a rotation of the material body (the background face-centered cubic lattice), we investigate elastic properties of Model I in the absence of \mathbf{H} as shown in (b). In contrast, an external field is persistently required to retain the dipole moments for paramagnetic particles (Model II) as described in (c). In this case, the system is no longer invariant under rotation with respect to the external field \mathbf{H} because the dipole moments of magnetic particles do not rotate along with the rotation of the lattice. Note that the (0,0,1)-orientation of the FCC lattice is directed along the external field in this illustration. We also study the case where the (1,1,1)-orientation of the FCC lattice is directed along \mathbf{H} .

As for the orientation of the system, we consider two cases in which the (0,0,1)- and (1,1,1)-orientations of the FCC lattice are directed along the z -axis.³⁶ When the lattices are elongated or contracted along the z -direction due to the anisotropic magnetic interaction, the resultant lattices of the (0,0,1)- and (1,1,1)-cases are tetragonal and rhombohedral, respectively.

Finally, we assume that our model system is incompressible, i.e., the volume of the whole system is fixed and persists even under deformations. Here, we set $V = (\sqrt{2}/2)a_{\text{el}}^3N$, at which the total Hamiltonian \mathcal{H}_{tot} is minimized for $m = 0$.

III. DENSITY FUNCTIONAL THEORY: BRIDGING SCALES

We then formulate a density functional theory (DFT) for the dipole-spring model by approximating the free-energy functional $\mathcal{F}[\rho(\mathbf{r})]$, where $\rho(\mathbf{r})$ denotes the one-body density field of the magnetic particles. Together with the ideal gas term

$$\mathcal{F}^{\text{id}}[\rho(\mathbf{r})] = \beta^{-1} \int d\mathbf{r} \rho(\mathbf{r}) [\ln\{\Lambda^3 \rho(\mathbf{r})\} - 1], \quad (6)$$

where $\beta \equiv (k_B T)^{-1}$ is the inverse temperature, the total free-energy functional subjected to minimization is given as

$$\mathcal{F}[\rho(\mathbf{r})] = \mathcal{F}^{\text{id}}[\rho(\mathbf{r})] + \mathcal{F}^{\text{ex}}[\rho(\mathbf{r})], \quad (7)$$

where $\mathcal{F}^{\text{ex}}[\rho(\mathbf{r})]$ denotes the excess functional describing the interparticle interactions (1). Following Ref. 70, we employ the Picard iteration algorithm

$$\rho^{(i+1)}(\mathbf{r}) = \alpha \hat{\rho}^{(i)}(\mathbf{r}) + (1 - \alpha) \rho^{(i)}(\mathbf{r}), \quad (8)$$

with a mixing parameter α and

$$\tilde{\rho}^{(i)}(\mathbf{r}) = \exp\left(-\beta \frac{\delta \mathcal{F}^{\text{ex}}}{\delta \rho^{(i)}(\mathbf{r})} + \beta \mu_i\right), \quad (9)$$

where

$$\mu_i \equiv \frac{1}{V_{\text{cell}}} \int_{\text{cell}} d\mathbf{r} \left[\ln\{\rho^{(i)}(\mathbf{r})\Lambda^3\} - \frac{\delta \mathcal{F}^{\text{ex}}}{\delta \rho^{(i)}(\mathbf{r})} \right], \quad (10)$$

which is updated in each iteration step to ensure that the total (average) number of particles is kept fixed. Accordingly, for the verification of successful minimization, we use the relative chemical potential defined as

$$\Delta\mu_{\text{rel}} \equiv \frac{\mu_{i+1} - \mu_i}{\mu_{i+1}}. \quad (11)$$

In this way, \mathcal{F} is minimized for a prescribed value of the vacancy concentration n_{vac} . In principle, our model systems are defect-free, i.e., $n_{\text{vac}} = 0$. To accelerate and enhance the robustness of the minimization processes, however, we consider lattices with vacancy concentration of $n_{\text{vac}} = 0.001 \pm 10^{-6}$.

Regarding the geometry of the calculation box, we use the primitive unit cell in our calculations, consisting of only one particle, instead of the cubic unit cell of the FCC lattice, consisting of four particles, usually adopted in DFT studies of freezing. Accordingly, we use periodic boundary conditions in the directions of three primitive vectors. Both expressions for the primitive and corresponding reciprocal lattice vectors can be found in [Appendix A](#). With this geometry, we are able to minimize our free-energy functional more precisely ($\Delta\mu_{\text{rel}} < 10^{-15}$ in most cases), compared to the method using the cubic unit cell ($\Delta\mu_{\text{rel}} \approx 10^{-8}$ for the tested cases). In principle, our DFT model could also be used to investigate additional structure formations involving more than a single particle in a larger calculation box. Such an extension, however, would require a more complicated pseudospring potential than the one we employ here (see [Sec. III B](#) for more details) and, therefore, goes beyond the scope of this study.

Now we turn to the excess functional $\mathcal{F}^{\text{ex}}[\rho(\mathbf{r})]$, which is given as a sum of three functionals corresponding to the steric repulsion, magnetic dipole–dipole interaction, and harmonic spring potential. First, for the hard-core repulsion, we use the White-Bear II (WB-II) functional⁷¹ with the Tarazona tensors,⁷² which is one of the most precise versions among the fundamental measure theory for hard spheres.⁷³ Then, for the elastic and magnetic dipole–dipole interactions, we intend to adopt the simple mean-field functional in the form of

$$\mathcal{F}_{\text{MF}}[\rho(\mathbf{r})] \equiv \frac{1}{2} \int d\mathbf{r} \int d\mathbf{r}' \rho(\mathbf{r}) u(\mathbf{r} - \mathbf{r}') \rho(\mathbf{r}'), \quad (12)$$

where $u(\mathbf{r})$ is an appropriate pair potential. However, the practical evaluation of the above functionals is not straightforward. In what follows, we describe how to construct the Fourier transforms of the elastic and magnetic energies, which allow us to perform DFT calculations in Fourier space.

A. Magnetic dipolar interaction

As discussed, there are two important properties inherent in the magnetic dipole–dipole interaction [Eq. (5)] in three dimensions.

It is long-range and anisotropic,⁷⁴ which has to be taken into account in DFT calculations.

When we switch from $m = 0$ to $m \neq 0$ in the initial orientation, the systems elongate or contract along the direction of \mathbf{m} , i.e., \hat{z} , and so does the unit cell. Then, the side lengths of the cubic unit cell are no longer the same, but satisfy the relation $a_x = a_y \neq a_z$, where a_x , a_y , and a_z denote the side lengths in the x -, y -, and z -direction, respectively. Here, we define the aspect ratio as $R_{\text{asp}} \equiv a_z/a_x$. We note that R_{asp} characterizes the deformation of the internal lattice structure.

Now, we address the long-range nature of the magnetic dipole–dipole interaction in three dimensions. The difficulty arises from the fact that the interaction energy, i.e., the integral of u_m , diverges at both short and long distances. In our DFT calculation, this issue can be resolved rather easily. On the one hand, the steric repulsion hinders particles from approaching closer than their diameter and therefore prevents the divergence at short distances. On the other hand, as the DFT calculation is performed in Fourier space, the divergence at long distance can be handled directly as follows. While, for $\mathbf{k} \neq 0$ Fourier modes, the Fourier transform of the dipole–dipole interaction can be obtained with the aid of the orthogonality of the spherical harmonics Y_l^m , the $\mathbf{k} = 0$ mode, which dictates the long-range divergence, indeed depends on the shape of the whole material body (see [Appendix B](#) for more details). With such a shape dependent mode, which is related to the demagnetizing factor in continuum theory,⁶¹ we are able to capture the long-ranged nature of the magnetic interaction. In general, we may consider a system with the initially spheroidal shape (at $m = 0$) of the shape parameter $R_{\text{sh}} \equiv R_z/R_x$, where $R_x = R_y$ and R_z are the lengths of the semiaxes along the x -, y -, and z -axis, respectively. In contrast to R_{asp} , here R_{sh} indicates the aspect ratio of the whole material. As we turn on the magnetic interaction applying a magnetic field, the *initial* aspect ratio of the whole system shape further changes to $R_{\text{asp}}R_{\text{sh}}$ due to magnetostriction associated with a change in internal lattice structure.

B. Elastic energy

While the magnetic particles are strictly labeled due to fixation by the surrounding polymer matrix, namely, the elastic interaction term given in Eq. (3), the conventional machinery of DFT calculation assumes the indistinguishability of particles, i.e., as if the potential u_{el} was acting equally between all pairs of particles throughout the system. To nevertheless enable DFT calculations, a mapping of the harmonic spring potential onto a pseudospring potential u_{pseudo} has been proposed in [Ref. 24](#). There, only nearest-neighbor pairs of the resulting configuration are within the range of u_{pseudo} and thus elastically coupled to each other, as in the original system based on the harmonic springs [see Eq. (3)]. In the present study, the mapping is extended to three dimensions. Notably, in two and three spatial dimensions, the success of applying the finite-ranged pseudospring potential is connected to the particle arrangement arising from a freezing transition,⁴⁹ which has been extensively investigated within density functional approaches.^{75–79} Specifically, we consider the pseudospring potential

$$u_{\text{pseudo}}(r) = \begin{cases} \frac{1}{2} k_{\text{el}} (r - a_{\text{el}})^2 - u_0, & r < R_c, \\ 0 & \text{otherwise.} \end{cases} \quad (13)$$

In this expression, R_c and u_0 denote the cut-off length and the offset for the pseudospring potential, respectively. The cutoff length R_c is determined from corresponding Monte Carlo simulations as the distance at which the pair correlation function $g(r)$ is minimized, which turns out to be $R_c = 1.21a_{el}$. The value of u_0 is determined within the DFT calculations so as to match the vacancy concentration of the resultant lattice with the prescribed value of $n_{vac} = 0.001$.

The obtained u_{pseudo} instead of u_{el} is inserted into Eq. (12) via u . We refer to our previous study⁴⁹ for the detailed description and verification of the mapping of the real onto the pseudospring potential. Moreover, due to the anisotropy of dipolar interactions as discussed in Sec. III A, corresponding lattice structures may become anisotropic as well. Such anisotropy then should also be taken into account when we construct the pseudospring potential. In practice, we cut the spring potential at the surface of the spheroid with the aspect ratio R_{asp} , instead of at the surface of the sphere with the radius R_c as in Eq. (13). In other words, the cutting is direction-dependent. The resultant Fourier components are explicitly presented in Appendix C.

IV. MACROSCOPIC PARAMETERS

A. Nonlinear deformations

Now we consider macroscopic continuum parameters. To this end, we must first address the assumed volume conservation when developing our macroscopic description. While our model system is initialized with the prescribed volume V at $m = 0$, an external magnetic field induces a magnetostrictive effect, which is not necessarily volume preserving. However, the imposed incompressibility constraint hinders the system to relax to a new volume upon magnetization. Such effects introduce a predeformation hidden behind the maintained volume, rendering our model system nonlinear elastic. Here, following the group theoretical approach proposed in Ref. 80, we consider nonlinear elastic responses of our model system and calculate elastic moduli accordingly. For self-containedness, we briefly summarize the formulation and introduce the second-order corrections to the deformation gradient tensors that are relevant for the computation of elastic moduli.

Under the incompressibility condition, the deformation gradients in three dimensions are elements of the special linear group $SL(3, \mathbb{R})$, the Lie algebra of which is $sl(3, \mathbb{R})$. Generally, the components of the deformation gradient tensor \mathbf{F} are defined by $\mathbf{F}_{ij} = \partial \mathbf{r}'_i / \partial \mathbf{r}_j$, where \mathbf{r}' and \mathbf{r} mark the positions of the material elements in the deformed and undeformed state, respectively. Then nonlinear deformation gradient tensors \mathbf{F} may be expressed via the exponential map

$$\mathbf{F} = \exp\left(\sum_{i=1}^8 \epsilon_i \lambda_i\right), \quad (14)$$

where λ_i denote the $SL(3, \mathbb{R})$ group generators and ϵ_i are small coefficients indicating the magnitude of deformations generated by λ_i . One should choose a set of generators that is appropriate for the system considered. Accordingly, for our model system, we employ the generators of

$$\begin{aligned} \lambda_1 &= \begin{pmatrix} 1 & 0 & 0 \\ 0 & -1 & 0 \\ 0 & 0 & 0 \end{pmatrix}, & \lambda_2 &= \frac{1}{\sqrt{3}} \begin{pmatrix} 1 & 0 & 0 \\ 0 & 1 & 0 \\ 0 & 0 & -2 \end{pmatrix}, \\ \lambda_3 &= \begin{pmatrix} 0 & 0 & 0 \\ 0 & 0 & 1 \\ 0 & 1 & 0 \end{pmatrix}, & \lambda_4 &= \begin{pmatrix} 0 & 0 & 1 \\ 0 & 0 & 0 \\ 1 & 0 & 0 \end{pmatrix}, \\ \lambda_5 &= \begin{pmatrix} 0 & 1 & 0 \\ 1 & 0 & 0 \\ 0 & 0 & 0 \end{pmatrix}, & \lambda_6 &= \begin{pmatrix} 0 & 0 & 0 \\ 0 & 0 & -1 \\ 0 & 1 & 0 \end{pmatrix}, \\ \lambda_7 &= \begin{pmatrix} 0 & 0 & 1 \\ 0 & 0 & 0 \\ -1 & 0 & 0 \end{pmatrix}, & \lambda_8 &= \begin{pmatrix} 0 & -1 & 0 \\ 1 & 0 & 0 \\ 0 & 0 & 0 \end{pmatrix}. \end{aligned} \quad (15)$$

Here, the transformations associated with λ_1 stretch (compress) the system along the x -axis, combined with compressions (stretches) along the y -axis; the deformations generated by λ_2 stretch (compress) the system in the xy -plane combined with compressions (stretches) along the z -axis of twice the magnitude; λ_3 , λ_4 , and λ_5 generate shear deformations in the yz -, zx -, and xy -plane, respectively; λ_6 , λ_7 , and λ_8 generate rotations in the yz -, zx -, and xy -plane, respectively. We note that λ_1 can also be regarded as a generator of shear deformations in the xy -plane, but with orientations different from those generated by λ_5 . For the purpose of calculating elastic moduli, corrections up to the second order of ϵ_i are relevant. Accordingly, we may truncate the expansion at the third order of $\{\epsilon_i\}$ and use

$$\mathbf{F} = \mathbf{I} + \sum_i \epsilon_i \lambda_i + \frac{1}{2} \left(\sum_i \epsilon_i \lambda_i \right) \cdot \left(\sum_j \epsilon_j \lambda_j \right). \quad (16)$$

We note that, in general, generators do not commute, i.e., $\lambda_i \cdot \lambda_j \neq \lambda_j \cdot \lambda_i$. Within our approach, the free-energy density \mathcal{F} (see Sec. III for the definition based on density functional theory), equivalent to the deformation energy density in nonlinear elasticity, is regarded as a function of $\{\epsilon_i\}$. This choice naturally allows us to define the generalized elastic moduli as

$$C_{ij} = \frac{\partial^2 \mathcal{F}}{\partial \epsilon_i \partial \epsilon_j}. \quad (17)$$

From our DFT, we determine the elastic constants C_{ij} explicitly by deforming the primitive unit cell. Numerically, we first transform the primitive vectors via corresponding deformation gradient tensors \mathbf{F} and obtain the associated reciprocal lattice vectors in deformed states up to the second order, which are presented in Appendix A. Minimizing our density functional under deformations, we then calculate free energies $\mathcal{F}(\{\epsilon_i\})$, with which second derivatives can be obtained through finite differences when

compared to the free energy of the reference (undeformed) state. Specifically, we obtain the diagonal terms of the stiffness tensor from

$$C_{ii} = \left(\frac{\partial^2 \mathcal{F}}{\partial \epsilon_i^2} \right) \approx \frac{\mathcal{F}(\epsilon_i) + \mathcal{F}(-\epsilon_i) - 2\mathcal{F}(0)}{\epsilon_i^2}, \quad (18)$$

while the off-diagonal terms can be calculated as

$$C_{ij} = \left(\frac{\partial^2 \mathcal{F}}{\partial \epsilon_i \partial \epsilon_j} \right) \approx \frac{\mathcal{F}(\epsilon_i, \epsilon_j) + \mathcal{F}(-\epsilon_i, -\epsilon_j) - \mathcal{F}(-\epsilon_i, \epsilon_j) - \mathcal{F}(\epsilon_i, -\epsilon_j)}{4\epsilon_i \epsilon_j}. \quad (19)$$

In most of the cases, we use $\epsilon_1 = \epsilon_2/\sqrt{3} = \epsilon_3 = \dots = \epsilon_7 = 0.0001$, except for the cases of the (1,1,1)-orientation with $\eta = 0.3$ and $m \leq 2.5$, in which the functional can be minimized down to the values of $\Delta\mu_{\text{rel}}$ between 10^{-4} and 10^{-8} at most. There, we use two different values of $\epsilon_1 = \epsilon_2/\sqrt{3} = \epsilon_3 = \dots = \epsilon_7 = 0.0001$ and 0.001 to calculate elastic coefficients and confirm that these values lead to consistent results.

In the case of Model I, only the five generators λ_i for $i = 1, \dots, 5$ are relevant, among which the shear deformations generated by λ_3 and λ_4 lead to identical contributions to \mathcal{F} due to the symmetry of tetragonal and rhombohedral lattices. In addition to those, the relative rotations corresponding to λ_6 and λ_7 must be included for the description of Model II, whereas rotations in the xy -plane generated by λ_8 are still irrelevant. Again due to the symmetry, the rotations corresponding to λ_6 and λ_7 lead to identical contributions to \mathcal{F} .

Before proceeding to the results, we note that some coefficients vanish and others are equal to each other due to the underlying symmetries of the considered lattice. In linear elasticity, an irreducible representation of stiffness tensors allows us to determine nonzero and equal elastic constants, which can also be extended to our group theoretical approach, as discussed in Appendix D. The macroscopic approach described here provides a precise and economic framework to investigate nonlinear elastic properties of incompressible anisotropic systems. In particular, our choice of generators given by Eq. (15) and the corresponding stiffness tensors given in Eqs. (D5) and (D7), respectively, determine all the necessary and allowed deformations and elastic constants compatible with the underlying symmetry of the system and the imposed constraint. For instance, in Figs. 3(b) and 3(f) for rhombohedral lattices, we confirm that $C_{11} = C_{55}$ and $C_{13} = C_{45}$, respectively, in accordance with Eq. (D7). Accordingly, in Secs. IV C and IV D, we only discuss elastic moduli and rotation coefficients that are nonzero in irreducible representation.

We stress that a nonlinear framework as outlined by Eq. (16) is necessary to obtain appropriate results. Sticking to the linear strain tensors as given by Eq. (D1), instead of our nonlinear definition in Eq. (16), may involve errors in the second order, which are relevant for elastic constants. Indeed, the rotation coefficients C_{66} and C_{77} shown in Fig. 4(a) can become negative, if the volume conservation in the second order is not explicitly taken into account via Eqs. (14) and (15). Alternatively, one may consider the method of Lagrange multipliers, which is, however, technically demanding, particularly in combination with the density functional calculation.

From now on, we measure lengths and energies in units of the rest length a_{el} and the thermal energy $k_B T$, respectively. Accordingly, the magnitude m of the magnetic moment and the spring

constant k_{el} are measured in units of $m_0 \equiv \sqrt{k_B T a_{\text{el}}^3 / \mu_0}$ and $k_B T / a_{\text{el}}^2$, respectively. We consider systems with elastic constant $k_{\text{el}} = 100$ and shape parameter $R_{\text{sh}} = 1$, and we investigate the effects of magnetization on the mechanical properties by varying the magnitude of the magnetic moment m . The two models described in Sec. II give identical results as long as no rotations are considered, while only the paramagnetic Model II has a unique reference state with respect to rotations.

One can also probe steric effects by varying the volume packing fraction η . Naively speaking, while steric repulsion should affect the bulk modulus of a system, how and to what extent it would affect the mechanical properties under each specific deformation is still unclear. Moreover, there might also appear numerical artifacts due to several approximations employed. Therefore, leaving systematic investigations for further studies, we demonstrate that our method is valid for a reasonable range of η by employing two representative values of $\eta = 0.1$ and 0.3 , which are smaller than the coexisting fluid (crystal) packing fraction of 0.495 (0.544)⁷⁰ for the structural arrangement of the hard-core particles in the absence of elastic and magnetic interactions. We refer by those numerical values to the fluid–solid phase transition point for hard-sphere systems. Notably, the pseudospring potential suffices to stabilize the FCC crystal for $\eta = 0$ within our model when $m = 0$. Indeed, for zero or small m , steric effects seem to be negligible, as one can confirm from Fig. 2 (see Sec. IV B) as well as from Figs. 3 and 4 (see Sec. IV C). For large m , however, the steric repulsions turn out to play an important role, which we attribute to the fact that they prevent a divergence of magnetic dipolar interactions at short distance. We discuss this issue more in detail in Secs. IV C and IV D.

B. Magnetostriction

As a first step, we determine the reference equilibrium state of the undeformed system for a given magnetization m . Technically,

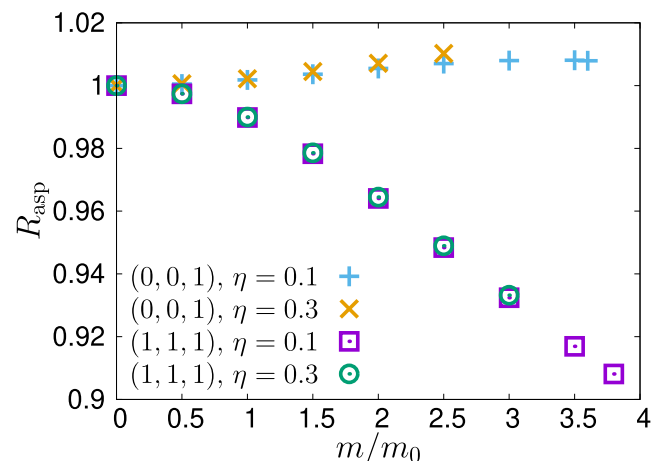


FIG. 2. The aspect ratio R_{asp} of the system is presented as a function of m measured in units of $m_0 = \sqrt{k_B T a_{\text{el}}^3 / \mu_0}$. Converse magnetostriction effects are observed, depending on the orientation of the lattice.

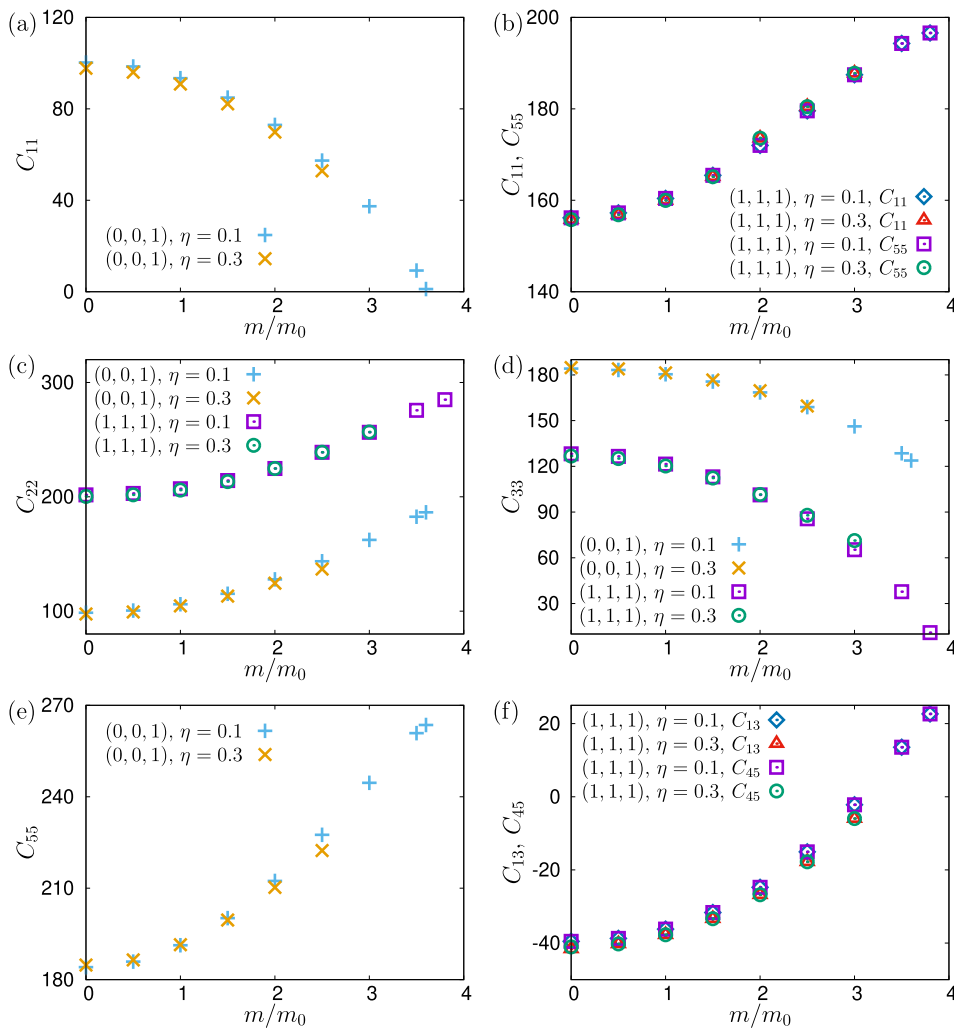


FIG. 3. Elastic coefficients are presented as functions of m . The values of (a) C_{11} for the (0,0,1)-orientation, (b) C_{11} and C_{55} for the (1,1,1)-orientation, (c) C_{22} for the (0,0,1)- and (1,1,1)-orientations, (d) C_{33} for the (0,0,1)- and (1,1,1)-orientations, (e) C_{55} for the (0,0,1)-orientation, and (f) C_{13} and C_{45} for the (1,1,1)-orientation are shown. For values of m larger than those presented in this figure, we were not able to find stable equilibrium configurations.

we first determine the value of u_0 for which the vacancy concentration of the system becomes equal to the prescribed value within the margin of tolerated error. Then, varying R_{asp} while fixing u_0 , we find the value of the aspect ratio R_{asp} at which the free-energy functional is minimized. The resultant values of R_{asp} are shown in Fig. 2.

The most prominent feature here is that the magnetostriction effects of the (0,0,1)- and (1,1,1)-orientations are opposite to each other. In line with the results reported in Ref. 36, our systems elongate when the dipole moments are directed along the (0,0,1)-orientation, while a contraction along the direction of the dipole moments is observed in the (1,1,1)-case, confirming that the internal configuration of magnetic particles is a decisive factor of the magnetostriction effect. In addition, we also note that the magnetostriction effect can be reversed, if large values of the shape parameter ($R_{\text{sh}} \gtrsim 2$) are used in the case of the (0,0,1)-orientation (results not shown). Such shape-dependence is a trivial consequence of the long-range nature of the dipolar interaction.

C. Elastic coefficients

First, we take a closer look at the elastic constant C_{55} , corresponding to shear deformations in the xy -plane, and C_{11} , corresponding to stretches (compressions) along the x -axis combined with compressions (stretches) along the y -axis. C_{11} can also be regarded as a shear modulus, but corresponding to shear deformations with orientations different from those for C_{55} . In most cases, the dipolar interaction, which is repulsive in the plane perpendicular to the dipole moment, causes an increase of the elastic constants. Specifically, as shown in Fig. 3(b), values of both $C_{11} = C_{55}$ increase as m increases in the (1,1,1)-case. In the (0,0,1)-case, only C_{55} is an increasing function of m , as shown in Fig. 3(e), while C_{11} in the (0,0,1)-case is a decreasing function of m , as shown in Fig. 3(a). Furthermore, as m increases further, C_{11} drops toward zero, indicating instability of the tetragonal lattices. We notice here that hexagonal configurations can be obtained eventually by squeezing the tetragonal lattice in the xy -plane, if the whole lattice is projected on the

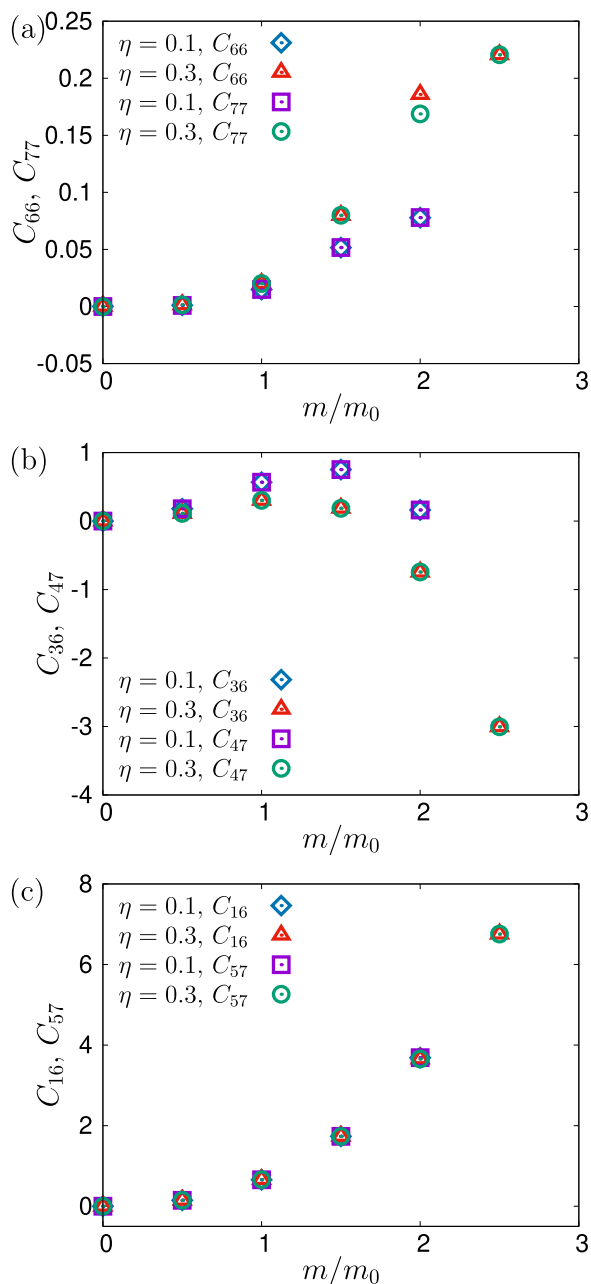


FIG. 4. Rotation coefficients obtained from the (1,1,1)-orientation. In (a), the coefficients C_{66} and C_{77} , respectively, corresponding solely to the rotations in the yz - and xz -planes are presented, whereas the off-diagonal coefficients C_{36} and C_{47} as well as C_{16} and C_{57} are depicted in (b) and (c), respectively.

xy -plane. In other words, as m increases, there might arise a growing tendency to match the lattice to the underlying symmetry of the magnetic dipole-dipole interaction, which prefers the hexagonal lattice over the tetragonal lattice in the plane perpendicular to the dipole moment. Therefore, we conclude that such a softening

effect correlates with a rearrangement of the magnetic particles in the plane perpendicular to \mathbf{m} .

Next we turn to the elastic constants of C_{22} , corresponding to stretches (compressions) in the xy -plane combined with compressions (stretches) along the z -axis of twice the magnitude, and C_{33} , corresponding to shear deformation in the yz -plane (or equivalently C_{44} , corresponding to shear deformations in the xz -plane). All of them involve deformations in the z -direction. In both the (0,0,1)- and (1,1,1)-orientations, C_{22} is an increasing function of m [Fig. 3(c)], indicating hardening of the materials. Since there is no significant difference between the systems of $\eta = 0.1$ and 0.3, the phenomenon of hardening observed here has a purely elastic origin. Simultaneously, C_{33} is always a decreasing function of m [Fig. 3(d)]. Moreover, at large m , the rhombohedral lattice becomes unstable as well, with the values of C_{33} dropping toward zero. Such instabilities at large m and the decrease of C_{33} , in general, may originate from the tendency toward pair formation^{20,81} or similarly from the typical chain-like aggregates forming under strong dipolar interactions.^{48,82,83} Indeed, we observe a shift of the energetic minimum in the landscape of two-body interaction energy from separated to touching configurations between $m = 2.5$ and 3.0 in the (1,1,1)-case (not shown). This seems to confirm that the instability is the consequence of the formation of touching pairs. In the case of the (0,0,1)-orientation, the drop toward zero in C_{11} occurs in advance of that in C_{33} [compare Figs. 3(a) and 3(d)], indicating that rearrangement in the xy -plane is preferred over rearrangement in the z -direction. In stark contrast to the hardening in C_{22} , the onset of the instability accompanied with the softening depends on η significantly, which seems reasonable as the formation of pairs should always involve an interplay between attractive magnetic forces along the dipole orientations and repulsive steric forces. The hard-core repulsion prevents a divergence of attractive magnetic dipolar interactions, but touching of neighboring particles may still occur due to thermal fluctuations. Therefore, we conclude that for large m where the instability may develop, entropic contributions should be relevant for elastic properties of dipole-spring systems, verifying the utility of our DFT approach.

Finally, the values of C_{13} and C_{45} in the (1,1,1)-case are presented in Fig. 3(f). Overall they exhibit a similar behavior, increasing from negative values for small m to positive ones for large m . We note, however, that these constants reflect a rather specific symmetry inherent in the lattice and, therefore, may not reflect the situation of real magnetic gels.

D. Rotation coefficients

Finally, we investigate the rotation coefficients, which are relevant only in Model II. Alike the elastic constants, the rotation coefficients are calculated from Eqs. (18) and (19). As the (0,0,1)-orientation turns out to be unstable with respect to rotations in xz - and yz -planes, we only analyze the results for the (1,1,1)-orientation.

First, the coupling of the model systems to the applied magnetic field is captured by the rotation coefficients C_{66} and C_{77} , corresponding to rotations in the yz - and xz -plane, respectively. As shown in Fig. 4(a), the values of C_{66} and C_{77} increase as m increases, indicating an enhanced resistance to the rotations. Notably, we

observe discrepancies between the rotation coefficients at $\eta = 0.1$ and 0.3 , which again demonstrate the relevance of hard-core repulsions.

As shown in Fig. 4(b), the mixed coefficients of C_{36} and C_{47} , corresponding to mixed shear deformations and rotations in the yz - and xz -plane, respectively, first exhibit an increase as a function of m for small values of m . Then, the increasing trend is reversed for large m . We note that, in Ref. 48, where chain-like aggregates are assumed, only a decreasing tendency in the form of $-m^2$ has been predicted for D_2 , which is related to C_{36} and C_{47} in the present study. Presumably, as already mentioned for magnetostrictive effects in Sec. IV B, different behaviors may be due to the internal configuration of the magnetic particles. We also note that the values of C_{66} and C_{77} are $\sim 10^3$ times smaller than those of C_{33} and C_{44} . In Ref. 48, the rotation coefficient D_1 (related to C_{66} and C_{77} in the present study) is even larger than Δc_5 (related to C_{33} and C_{44} in the present study). Again, this may be caused by the different internal structure, which is chain-like in Ref. 48.

Finally, the additional mixed coefficients C_{16} and C_{57} increase monotonically, as shown in Fig. 4(c), which seems to be a simple consequence of enhancement of both hardening in the xy -plane (C_{11} and C_{55}) and resistance to rotations in the xz - or yz -plane (C_{66} and C_{77}).

V. CONCLUSION

So far, we have constructed and evaluated a DFT for three-dimensional dipole-spring models, which bridges from the discretized mesoscopic model to a macroscopic elasticity theory of magnetic gels. Based on the scale-bridging description, we have determined the elastic and rotational material coefficients. They depend on the mesoscopic configuration of the magnetic particles. Notably, we have observed softening responses to magnetization both in the external field direction and in the plane perpendicular to the external field, which indicates a tendency toward an instability. We have proposed that such behaviors imply changes in overall symmetry, accompanied by rearrangement of magnetic particles. Such rearrangements might be decomposed into the formation of a hexagonal-like arrangement in the plane perpendicular to the magnetic field and pair formation along the magnetic field direction. To verify our conclusion, the decreasing behavior of C_{11} needs to be tested experimentally. Notably, in a previous study, where random configurations for magnetic particles are assumed [see Fig. 14(b) of Ref. 46], a decrease of the shear modulus has been observed, suggesting that the idea of rearrangement may also be valid for real magnetic gels with disordered configurations.

Conversely, one could equally well think about synthesizing a sample with the regular arrangement adopted in this study. In particular, the prescribed FCC-based connectivity shows certain characteristics as explained above. For instance, 6 among 12 nearest neighboring particles are located in the same plane perpendicular to the magnetization in the case of (1,1,1)-orientation, and, thereby, the repulsive interaction in the plane seems to dominate the response of the magnetic particles. This leads to the contraction along the magnetization direction. We note that there have been attempts to synthesize thin ferrogel films.⁸⁴ Since, in planar configurations, magnetic particles form hexagonal arrangements in the plane

perpendicular to the external magnetic field,⁸⁵ it would be possible to obtain ferrogel films with a hexagonal configuration in such a way. Then, by stacking two-dimensional layers, a magnetic gel with a three-dimensional hexagonal structure might be fabricated experimentally. Our results of the (1,1,1)-case may then provide insight into such systems.

At the same time, regarding future work on our theory, one important direction is to address systems with random configurations. An important additional ingredient to model the heterogeneity inherent in real samples is polydispersity of the magnetic particles.⁸⁶ The idea of the replica DFT^{87,88} might be used to address directly disordered configurations. Finally, dynamical density functional theory⁸⁹⁻⁹¹ should provide a route to investigate the dynamics of the systems.

ACKNOWLEDGMENTS

This work was supported by funding from the Deutsche Forschungsgemeinschaft (DFG) through the SPP 1681, Grant Nos. ME 3571/3-3 (A.M.M.) and LO 418/16-3 (H.L.). A.M.M. was supported by the DFG through Heisenberg Grant No. ME 3571/4-1.

AUTHOR DECLARATIONS

Conflict of Interest

The authors have no conflicts to disclose.

Author Contributions

Segun Goh: Conceptualization (equal); Data curation (lead); Formal analysis (lead); Investigation (lead); Methodology (lead); Software (lead); Validation (lead); Visualization (lead); Writing – original draft (lead); Writing – review & editing (lead). **Andreas M. Menzel:** Conceptualization (equal); Funding acquisition (equal); Methodology (supporting); Project administration (supporting); Supervision (supporting); Writing – review & editing (lead). **René Wittmann:** Conceptualization (supporting); Methodology (supporting); Writing – review & editing (supporting). **Hartmut Löwen:** Conceptualization (equal); Funding acquisition (equal); Methodology (supporting); Project administration (lead); Resources (lead); Supervision (lead); Writing – review & editing (supporting).

DATA AVAILABILITY

The data that support the findings of this study are available from the corresponding author upon reasonable request.

APPENDIX A: RECIPROCAL LATTICES

For the (0,0,1)-, and (1,1,1)-orientations of the FCC lattice, the primitive vectors read

$$\mathbf{a}_1 = \frac{a}{2}(\hat{x} + \hat{y}), \quad \mathbf{a}_2 = \frac{a}{2}(\hat{y} + \hat{z}), \quad \mathbf{a}_3 = \frac{a}{2}(\hat{z} + \hat{x}) \quad (\text{A1})$$

and

$$\begin{aligned} \mathbf{a}_1 &= \frac{a}{2} \left(\frac{2}{\sqrt{6}} \hat{y} + \frac{2}{\sqrt{3}} \hat{z} \right), \\ \mathbf{a}_2 &= \frac{a}{2} \left(-\frac{1}{\sqrt{2}} \hat{x} - \frac{1}{\sqrt{6}} \hat{y} + \frac{2}{\sqrt{3}} \hat{z} \right), \\ \mathbf{a}_3 &= \frac{a}{2} \left(\frac{1}{\sqrt{2}} \hat{x} - \frac{1}{\sqrt{6}} \hat{y} + \frac{2}{\sqrt{3}} \hat{z} \right), \end{aligned} \quad (\text{A2})$$

respectively. Here, $a = \sqrt{2}a_{\text{cl}}$ denotes the side length of the cubic unit cell.

In practice, the DFT calculations are performed with the reciprocal lattice vectors in Fourier space. For the (0,0,1)-orientation, the reciprocal vectors read

$$\begin{aligned} \mathbf{b}_1 &= \frac{2\pi}{a} (1, 1, -1), \\ \mathbf{b}_2 &= \frac{2\pi}{a} (-1, 1, 1), \\ \mathbf{b}_3 &= \frac{2\pi}{a} (1, -1, 1), \end{aligned} \quad (\text{A3})$$

while for the (1,1,1)-orientation, we obtain

$$\begin{aligned} \mathbf{b}_1 &= \frac{2\pi}{a} \left(0, \frac{4}{\sqrt{6}}, \frac{1}{\sqrt{3}} \right), \\ \mathbf{b}_2 &= \frac{2\pi}{a} \left(-\sqrt{2}, -\frac{2}{\sqrt{6}}, \frac{1}{\sqrt{3}} \right), \\ \mathbf{b}_3 &= \frac{2\pi}{a} \left(\sqrt{2}, -\frac{2}{\sqrt{6}}, \frac{1}{\sqrt{3}} \right). \end{aligned} \quad (\text{A4})$$

Under deformation, the reciprocal vectors are transformed accordingly. We expand the reciprocal vectors of deformed lattices with respect to $\{\epsilon_i\}$ to compute the corresponding reciprocal lattice vectors in the form

$$\begin{aligned} \mathbf{b}_1^{\text{deformed}} &= \mathbf{b}_1 + \frac{2\pi}{a} \Delta \mathbf{b}_1, \\ \mathbf{b}_2^{\text{deformed}} &= \mathbf{b}_2 + \frac{2\pi}{a} \Delta \mathbf{b}_2, \\ \mathbf{b}_3^{\text{deformed}} &= \mathbf{b}_3 + \frac{2\pi}{a} \Delta \mathbf{b}_3. \end{aligned} \quad (\text{A5})$$

The correction terms $\Delta \mathbf{b}_1$, $\Delta \mathbf{b}_2$, and $\Delta \mathbf{b}_3$ for the (0,0,1)- and (1,1,1)-cases are given in [Tables I](#) and [II](#), respectively, which are sufficient

TABLE I. Reciprocal lattice vectors for the (0,0,1)-orientation. As for the infinitesimal parameters $\{\epsilon_i\}$, see Eqs. (14) and (15) in which the deformation gradient tensor as well as the generators are defined.

ϵ	$\Delta \mathbf{b}_1$	$\Delta \mathbf{b}_2$	$\Delta \mathbf{b}_3$
ϵ_1	$(-\epsilon + \frac{1}{2}\epsilon^2, \epsilon + \frac{1}{2}\epsilon^2, 0)$	$(\epsilon - \frac{1}{2}\epsilon^2, \epsilon + \frac{1}{2}\epsilon^2, 0)$	$(-\epsilon + \frac{1}{2}\epsilon^2, -\epsilon - \frac{1}{2}\epsilon^2, 0)$
ϵ_2	$(-\frac{1}{\sqrt{3}}\epsilon + \frac{1}{6}\epsilon^2, -\frac{1}{\sqrt{3}}\epsilon + \frac{1}{6}\epsilon^2, -\frac{2}{\sqrt{3}}\epsilon - \frac{2}{3}\epsilon^2)$	$(\frac{1}{\sqrt{3}}\epsilon - \frac{1}{6}\epsilon^2, -\frac{1}{\sqrt{3}}\epsilon + \frac{1}{6}\epsilon^2, \frac{2}{\sqrt{3}}\epsilon + \frac{2}{3}\epsilon^2)$	$(-\frac{1}{\sqrt{3}}\epsilon + \frac{1}{6}\epsilon^2, \frac{1}{\sqrt{3}}\epsilon - \frac{1}{6}\epsilon^2, \frac{2}{\sqrt{3}}\epsilon + \frac{2}{3}\epsilon^2)$
ϵ_3	$(0, \epsilon + \frac{1}{2}\epsilon^2, -\epsilon - \frac{1}{2}\epsilon^2)$	$(0, -\epsilon + \frac{1}{2}\epsilon^2, -\epsilon + \frac{1}{2}\epsilon^2)$	$(0, -\epsilon - \frac{1}{2}\epsilon^2, \epsilon + \frac{1}{2}\epsilon^2)$
ϵ_4	$(\epsilon + \frac{1}{2}\epsilon^2, 0, -\epsilon - \frac{1}{2}\epsilon^2)$	$(-\epsilon - \frac{1}{2}\epsilon^2, 0, \epsilon + \frac{1}{2}\epsilon^2)$	$(-\epsilon + \frac{1}{2}\epsilon^2, 0, -\epsilon + \frac{1}{2}\epsilon^2)$
ϵ_5	$(-\epsilon + \frac{1}{2}\epsilon^2, -\epsilon + \frac{1}{2}\epsilon^2, 0)$	$(-\epsilon - \frac{1}{2}\epsilon^2, \epsilon + \frac{1}{2}\epsilon^2, 0)$	$(\epsilon + \frac{1}{2}\epsilon^2, -\epsilon - \frac{1}{2}\epsilon^2, 0)$
ϵ_6	$(0, -\epsilon - \frac{1}{2}\epsilon^2, -\epsilon + \frac{1}{2}\epsilon^2)$	$(0, \epsilon - \frac{1}{2}\epsilon^2, -\epsilon - \frac{1}{2}\epsilon^2)$	$(0, \epsilon + \frac{1}{2}\epsilon^2, \epsilon - \frac{1}{2}\epsilon^2)$
ϵ_7	$(-\epsilon - \frac{1}{2}\epsilon^2, 0, -\epsilon + \frac{1}{2}\epsilon^2)$	$(\epsilon + \frac{1}{2}\epsilon^2, 0, \epsilon - \frac{1}{2}\epsilon^2)$	$(\epsilon - \frac{1}{2}\epsilon^2, 0, -\epsilon - \frac{1}{2}\epsilon^2)$

TABLE II. Reciprocal lattice vectors for the (1,1,1)-orientation. The deformation gradient tensor and the group generators corresponding to the infinitesimal parameters $\{\epsilon_i\}$ are defined in Eqs. (14) and (15).

ϵ	$\Delta \mathbf{b}_1$	$\Delta \mathbf{b}_2$	$\Delta \mathbf{b}_3$
ϵ_1	$(0, \frac{4}{\sqrt{6}}\epsilon + \frac{2}{\sqrt{6}}\epsilon^2, 0)$	$(\sqrt{2}\epsilon - \frac{\sqrt{2}}{2}\epsilon^2, -\frac{2}{\sqrt{6}}\epsilon - \frac{1}{\sqrt{6}}\epsilon^2, 0)$	$(-\sqrt{2}\epsilon + \frac{\sqrt{2}}{2}\epsilon^2, -\frac{2}{\sqrt{6}}\epsilon - \frac{1}{\sqrt{6}}\epsilon^2, 0)$
ϵ_2	$(0, -\frac{2\sqrt{2}}{3}\epsilon + \frac{\sqrt{6}}{9}\epsilon^2, \frac{2}{3}\epsilon + \frac{2\sqrt{3}}{9}\epsilon^2)$	$(\frac{\sqrt{6}}{3}\epsilon - \frac{\sqrt{2}}{6}\epsilon^2, \frac{\sqrt{2}}{3}\epsilon - \frac{\sqrt{6}}{18}\epsilon^2, \frac{2}{3}\epsilon + \frac{2\sqrt{3}}{9}\epsilon^2)$	$(-\frac{\sqrt{6}}{3}\epsilon + \frac{\sqrt{2}}{6}\epsilon^2, \frac{\sqrt{2}}{3}\epsilon - \frac{\sqrt{6}}{18}\epsilon^2, \frac{2}{3}\epsilon + \frac{2\sqrt{3}}{9}\epsilon^2)$
ϵ_3	$(0, -\frac{1}{\sqrt{3}}\epsilon + \frac{2}{\sqrt{6}}\epsilon^2, -\frac{4}{\sqrt{6}}\epsilon + \frac{\sqrt{3}}{6}\epsilon^2)$	$(0, -\frac{1}{\sqrt{3}}\epsilon - \frac{1}{\sqrt{6}}\epsilon^2, +\frac{2}{\sqrt{6}}\epsilon + \frac{\sqrt{3}}{6}\epsilon^2)$	$(0, -\frac{1}{\sqrt{3}}\epsilon - \frac{1}{\sqrt{6}}\epsilon^2, \frac{2}{\sqrt{6}}\epsilon + \frac{\sqrt{3}}{6}\epsilon^2)$
ϵ_4	$(-\frac{1}{\sqrt{3}}\epsilon, 0, \frac{\sqrt{3}}{6}\epsilon^2)$	$(-\frac{1}{\sqrt{3}}\epsilon - \frac{1}{\sqrt{2}}\epsilon^2, 0, \sqrt{2}\epsilon + \frac{\sqrt{3}}{6}\epsilon^2)$	$(-\frac{1}{\sqrt{3}}\epsilon + \frac{1}{\sqrt{2}}\epsilon^2, 0, -\sqrt{2}\epsilon + \frac{\sqrt{3}}{6}\epsilon^2)$
ϵ_5	$(-\frac{4}{\sqrt{6}}\epsilon, \frac{2}{\sqrt{6}}\epsilon^2, 0)$	$(\frac{2}{\sqrt{6}}\epsilon - \frac{1}{\sqrt{2}}\epsilon^2, \sqrt{2}\epsilon - \frac{1}{\sqrt{6}}\epsilon^2, 0)$	$(\frac{2}{\sqrt{6}}\epsilon + \frac{1}{\sqrt{2}}\epsilon^2, -\sqrt{2}\epsilon - \frac{1}{\sqrt{6}}\epsilon^2, 0)$
ϵ_6	$(0, \frac{1}{\sqrt{3}}\epsilon - \frac{2}{\sqrt{6}}\epsilon^2, -\frac{4}{\sqrt{6}}\epsilon - \frac{\sqrt{3}}{6}\epsilon^2)$	$(0, \frac{1}{\sqrt{3}}\epsilon + \frac{1}{\sqrt{6}}\epsilon^2, \frac{2}{\sqrt{6}}\epsilon - \frac{\sqrt{3}}{6}\epsilon^2)$	$(0, \frac{1}{\sqrt{3}}\epsilon + \frac{1}{\sqrt{6}}\epsilon^2, \frac{2}{\sqrt{6}}\epsilon - \frac{\sqrt{3}}{6}\epsilon^2)$
ϵ_7	$(\frac{1}{\sqrt{3}}\epsilon, 0, -\frac{\sqrt{3}}{6}\epsilon^2)$	$(\frac{1}{\sqrt{3}}\epsilon + \frac{1}{\sqrt{2}}\epsilon^2, 0, \sqrt{2}\epsilon - \frac{\sqrt{3}}{6}\epsilon^2)$	$(\frac{1}{\sqrt{3}}\epsilon - \frac{1}{\sqrt{2}}\epsilon^2, 0, -\sqrt{2}\epsilon - \frac{\sqrt{3}}{6}\epsilon^2)$

for the pure deformations that do not involve mixed terms, i.e., $\epsilon_i \epsilon_j$ for $i \neq j$. When more than two different types of deformations are applied, Eq. (14) still provides a correct formulation. However, such mixed terms are irrelevant for our incompressible systems because second-order corrections only enter via the diagonal terms in the stiffness tensor, as we describe in Appendix D (see Ref. 80 for details). Therefore, for the calculation of off-diagonal components in the stiffness tensors, we simply add the second-order corrections from two different types of pure deformations.

APPENDIX B: FOURIER TRANSFORM OF THE MAGNETIC DIPOLE-DIPOLE INTERACTION

1. Undeformed system

In the case of the $\mathbf{k} \neq 0$ terms, we calculate the Fourier transform utilizing the plane wave expansion

$$e^{i\mathbf{k}\cdot\mathbf{r}} = 4\pi \sum_{l=0}^{\infty} \sum_{m=-l}^l i^l j_l(kr) Y_l^m(\hat{\mathbf{k}}) Y_l^{m*}(\hat{\mathbf{r}}), \quad (\text{B1})$$

where j_l and Y_l^m are spherical Bessel functions and spherical harmonics, respectively, and the superscript asterisk $*$ denotes complex conjugate. Since the dipole-dipole interaction energy [Eq. (5)] is proportional to Y_2^0 for $\mathbf{m} = m\hat{z}$, i.e.,

$$u_m(\mathbf{r}) = \frac{\mu_0 m^2}{4\pi r^3} \left(-4\sqrt{\frac{\pi}{5}} \right) Y_2^0(\theta, \phi), \quad (\text{B2})$$

we obtain

$$\begin{aligned} \tilde{u}_m(\mathbf{k}) &= -\int_{\sigma}^{\infty} dr \int_0^{\pi} d\theta \int_0^{2\pi} d\phi \frac{\mu_0 m^2}{\pi} \sqrt{\frac{\pi}{5}} \frac{\sin \theta}{r} Y_2^0(\theta, \phi) e^{-i\mathbf{k}\cdot\mathbf{r}} \\ &= 4\mu_0 m^2 \sqrt{\frac{\pi}{5}} Y_2^0(\theta_k, \phi_k) \int_{\sigma}^{\infty} dr \frac{j_2(kr)}{r} \\ &= 4\mu_0 m^2 \sqrt{\frac{\pi}{5}} (1 - 3 \cos^2 \theta_k) \frac{k\sigma \cos k\sigma - \sin k\sigma}{k^3 \sigma^3}. \end{aligned} \quad (\text{B3})$$

Meanwhile, the $\mathbf{k} = 0$ term is calculated as follows:

$$\begin{aligned} \tilde{u}(\mathbf{k} = 0) &= \lim_{R \rightarrow \infty} \frac{\mu_0 m^2}{4\pi} 2\pi \int_0^{\pi} d\theta \int_{\sigma}^{R/\sqrt{\cos^2 \theta + \gamma^2 \sin^2 \theta}} dr r^2 \sin \theta \frac{1 - 3 \cos^2 \theta}{r^3} \\ &= \lim_{R \rightarrow \infty} \frac{\mu_0 m^2}{2} \int_0^{\pi} d\theta \sin \theta (1 - 3 \cos^2 \theta) \ln r_{\sigma}^{R/\sqrt{\cos^2 \theta + \gamma^2 \sin^2 \theta}} \\ &= -\frac{\mu_0 m^2}{2} \int_0^{\pi} d\theta \sin \theta (1 - 3 \cos^2 \theta) \ln \sqrt{\cos^2 \theta + \gamma^2 \sin^2 \theta} \\ &= \begin{cases} -\frac{\mu_0 m^2}{2} \left[\frac{2}{3} + \frac{2}{\gamma^2 - 1} - \frac{\gamma}{(\gamma^2 - 1)^{3/2}} \left(\sinh^{-1} \sqrt{\gamma^2 - 1} + \tanh^{-1} \sqrt{\frac{\gamma^2 - 1}{\gamma^2}} \right) \right], & \gamma > 1, \\ 0, & \gamma = 1, \\ -\frac{\mu_0 m^2}{2} \left[\frac{2}{3} + \frac{2}{\gamma^2 - 1} + \frac{\gamma}{(1 - \gamma^2)^{3/2}} \left(\sin^{-1} \sqrt{1 - \gamma^2} + \tan^{-1} \sqrt{\frac{1 - \gamma^2}{\gamma^2}} \right) \right], & \gamma < 1, \end{cases} \end{aligned} \quad (\text{B4})$$

where $\gamma = R_{\text{asp}} R_{\text{sh}}$. Apparently, the $\mathbf{k} = 0$ Fourier mode depends on the shape of systems, namely, the aspect ratio γ .

2. Deformed systems

When $\mathbf{k} \neq 0$, the Fourier transformation is shape independent. For the $\mathbf{k} = 0$ mode, however, the Fourier transform of the deformed system is, in general, different from the undeformed one, due to the dependence on the sample shape. To calculate the correction, we first clarify how a deformation \mathbf{F} modifies the integration via

$$\int_{\Omega(r, \theta, \phi)} d^3 r \frac{r^2 - 3z^2}{r^5} \rightarrow \int_{\Omega'(r, \theta, \phi)} d^3 r \frac{r'^2 - 3z'^2}{r'^5}, \quad (\text{B5})$$

where the prime indicates that the region of integration has been changed according to the deformation. Then, we recover the original shape of the system by changing the variables via $\mathbf{r}' = \mathbf{F} \cdot \mathbf{r}$ where the center dot \cdot denotes matrix multiplication, and subsequently, rewriting the integration as

$$\begin{aligned} \int_0^{\pi} d\theta \int_0^{2\pi} d\phi \int_{\sigma'(r, \theta, \phi)}^{R/\sqrt{\cos^2 \theta + \gamma^2 \sin^2 \theta}} dr r^2 \sin \theta \frac{(x'^2 + y'^2 - 2z'^2)}{r^2} \\ = \int_0^{\pi} d\theta U(\theta), \end{aligned} \quad (\text{B6})$$

while the boundaries of integration region stemming from the hard-core repulsion must be modified accordingly. We note that the differential $d^3 r = dr r^2 \sin \theta$ remains unchanged because $|\det \mathbf{F}| = 1$. Also note that $\mathbf{F} \equiv \partial \mathbf{r}' / \partial \mathbf{r}$. Then, the above integration can be performed up to the second order of $\{\epsilon_i\}$ with straightforward algebra, which has been performed using *Mathematica*.⁹² Here, with

$$U_0(\theta) = -\frac{\sin \theta - 3 \sin 3\theta}{16} \ln(\cos^2 \theta + \gamma^2 \sin^2 \theta), \quad (\text{B7})$$

we write the integrand in Eq. (B6) as

$$U(\theta) = U_0(\theta) + \Delta U(\theta, \{\epsilon_i\}), \quad (\text{B8})$$

where ΔU is the correction due to deformation.

First, for stretches (compressions) along the x -axis, combined with compressions (stretches) along the y -axis associated with λ_1 , ΔU reads

$$\begin{aligned} \Delta U(\theta, \epsilon_1) &= -\frac{\epsilon_1^2}{128} \sin^3 \theta [24 + 32 \cos 2\theta + 72 \cos 4\theta \\ &\quad + (99 + 180 \cos 2\theta + 105 \cos 4\theta) \ln(\cos^2 \theta + \gamma^2 \sin^2 \theta)] \\ &\equiv \Delta U_1(\theta, \epsilon_1). \end{aligned} \quad (\text{B9})$$

At the same time, the correction stemming from the deformation associated with λ_2 are already reflected in Eq. (B4), as we have calculated the values of $u_{\mathbf{m}}(\mathbf{k} = 0)$ for arbitrary aspect ratios. Because of the uniaxial symmetry of the magnetic dipolar interaction, the correction due to the shear deformations in the xy -plane takes the same form as Eq. (B9), namely, $\Delta U(\theta, \epsilon_5) = \Delta U_1(\theta, \epsilon_5)$. Next, the correction due to the shear deformations in the yz -plane is given as

$$\begin{aligned} \Delta U(\theta, \epsilon_3) &= \frac{\epsilon_3^2}{256} [36 \sin 3\theta + 28 \sin 5\theta - 72 \sin 7\theta \\ &\quad + (15 \sin \theta - 27 \sin 3\theta + 45 \sin 5\theta - 105 \sin 7\theta) \\ &\quad \times \ln(\cos^2 \theta + \gamma^2 \sin^2 \theta)] \\ &\equiv \Delta U_3(\theta, \epsilon_3). \end{aligned} \quad (\text{B10})$$

Due to the symmetry, we obtain $\Delta U(\theta, \epsilon_4) = \Delta U_3(\theta, \epsilon_4)$ for the shear deformation in the xz -plane. Now we turn to the deformations involving rotations. Again due to the uniaxial symmetry, the corrections due to the rotations in the xz - and yz -planes are identical with each other, reading

$$\begin{aligned} \Delta U(\theta, \epsilon_6) &= \frac{3\epsilon_6^2}{32} (\sin \theta - 3 \sin 3\theta) \ln(\cos^2 \theta + \gamma^2 \sin^2 \theta) \\ &\equiv \Delta U_6(\theta, \epsilon_6). \end{aligned} \quad (\text{B11})$$

For the off-diagonal terms, the form of ΔU is simply given as the sum of two deformations, except for the cases of C_{36} and C_{47} , in which the correction terms are given by

$$\begin{aligned} \Delta U(\theta, \epsilon_3, \epsilon_6) &= \Delta U_3(\theta, \epsilon_3) + \Delta U_6(\theta, \epsilon_6) \\ &\quad + \frac{\epsilon_3 \epsilon_6}{128} [28 \sin \theta + 18 \sin 3\theta - 42 \sin 5\theta \\ &\quad + (6 \sin \theta + 45 \sin 3\theta - 105 \sin 5\theta) \\ &\quad \times \ln(\cos^2 \theta + \gamma^2 \sin^2 \theta)] \\ &\equiv U_{36}(\theta, \epsilon_3, \epsilon_6) \end{aligned} \quad (\text{B12})$$

and

$$\Delta U(\theta, \epsilon_4, \epsilon_7) = \Delta U_{36}(\theta, \epsilon_4, \epsilon_7). \quad (\text{B13})$$

The appearance of the additional correction terms of $\epsilon_3 \epsilon_6$ and $\epsilon_4 \epsilon_7$ is the direct consequence of the uniaxial symmetry underlying the magnetic dipole-dipole interaction. Such corrections correspond to the only nonzero mixing terms associated with the shear deformation and the rotation in any plane parallel to the anisotropy axis of uniaxial systems, namely, the coefficient D_2 in Ref. 48. Moreover, equivalently to elastic constants as discussed in Appendix A, the corrections to $\tilde{u}(\mathbf{k} = 0)$ associated with mixing in the second order do not depend on nonlinear corrections in the deformation gradient \mathbf{F} . For the incompressibility constraint, they only appear at higher orders.

APPENDIX C: FOURIER TRANSFORM OF THE ANISOTROPIC PSEUDO-SPRING POTENTIAL

When $\mathbf{k} = 0$, the Fourier transformation can be performed analytically. In cylindrical coordinates, it reads

$$\begin{aligned} \tilde{u}_{\text{pseudo}}(\mathbf{k} = 0) &= 2\pi \int_{-R_{\text{asp}} R_c}^{R_{\text{asp}} R_c} dz \int_0^{\sqrt{R_c^2 - z^2 / R_{\text{asp}}^2}} d\rho \rho \left[\frac{1}{2} k_{\text{el}} (\sqrt{\rho^2 + z^2} - a_{\text{el}})^2 - u_0 \right] \\ &= 2\pi \int_{-R_{\text{asp}} R_c}^{R_{\text{asp}} R_c} dz \left[\frac{1}{8} k_{\text{el}} \rho^4 - \frac{1}{3} k_{\text{el}} a_{\text{el}} (\rho^2 + z^2)^{3/2} + \frac{1}{2} \rho^2 \left(\frac{1}{2} k_{\text{el}} z^2 + \frac{1}{2} k_{\text{el}} a_{\text{el}}^2 - u_0 \right) \right]_0^{\sqrt{R_c^2 - z^2 / R_{\text{asp}}^2}} \\ &= 4\pi \int_0^{R_{\text{asp}} R_c} dz \left[\frac{1}{8} k_{\text{el}} (R_c^2 - z^2 / R_{\text{asp}}^2)^2 - \frac{1}{3} k_{\text{el}} a_{\text{el}} (R_c^2 - z^2 / R_{\text{asp}}^2 + z^2)^{3/2} \right. \\ &\quad \left. + \frac{1}{3} k_{\text{el}} a_{\text{el}} z^3 + \frac{1}{2} \left(\frac{1}{2} k_{\text{el}} z^2 + \frac{1}{2} k_{\text{el}} a_{\text{el}}^2 - u_0 \right) (R_c^2 - z^2 / R_{\text{asp}}^2) \right], \end{aligned} \quad (\text{C1})$$

which can be evaluated straightforwardly, except for

$$\int_0^{R_{\text{asp}} R_c} dz (R_c^2 - z^2 / R_{\text{asp}}^2 + z^2)^{3/2} - z^3 = \frac{1}{8} R_{\text{asp}}^2 R_c^4 (3 + 2R_{\text{asp}}^2) + \frac{3}{8} R_{\text{asp}} R_c^4 \frac{\sinh^{-1} \sqrt{-1 + R_{\text{asp}}^2}}{\sqrt{-1 + R_{\text{asp}}^2}}. \quad (\text{C2})$$

Altogether, we obtain

$$\tilde{u}_{\text{pseudo}}(\mathbf{k} = 0) = \begin{cases} 2\pi \left[\frac{1}{15} R_{\text{asp}} (2 + R_{\text{asp}}^2) k_{\text{el}} R_c^5 - \frac{1}{4} \left(R_{\text{asp}}^2 + \frac{R_{\text{asp}} \sinh^{-1} \sqrt{-1 + R_{\text{asp}}^2}}{\sqrt{-1 + R_{\text{asp}}^2}} \right) k_{\text{el}} a_{\text{el}} R_c^4 \right. \\ \quad \left. + \frac{2}{3} R_{\text{asp}} \left(\frac{1}{2} k_{\text{el}} a_{\text{el}}^2 - u_0 \right) R_c^3 \right] - C_0, & R_{\text{asp}} > 1, \\ 4\pi \left[\frac{1}{10} k_{\text{el}} R_c^5 - \frac{1}{4} k_{\text{el}} R_c^4 a_{\text{el}} + \frac{1}{3} R_c^3 \left(\frac{1}{2} k_{\text{el}} a_{\text{el}}^2 - u_0 \right) \right] - C_0, & R_{\text{asp}} = 1, \\ 2\pi \left[\frac{1}{15} R_{\text{asp}} (2 + R_{\text{asp}}^2) k_{\text{el}} R_c^5 - \frac{1}{4} \left(R_{\text{asp}}^2 + \frac{R_{\text{asp}} \sin^{-1} \sqrt{1 - R_{\text{asp}}^2}}{\sqrt{1 - R_{\text{asp}}^2}} \right) k_{\text{el}} a_{\text{el}} R_c^4 \right. \\ \quad \left. + \frac{2}{3} R_{\text{asp}} \left(\frac{1}{2} k_{\text{el}} a_{\text{el}}^2 - u_0 \right) R_c^3 \right] - C_0, & R_{\text{asp}} < 1, \end{cases}$$

where

$$C_0 \equiv 4\pi \left[\frac{1}{10} k_{\text{el}} \sigma^5 - \frac{1}{4} k_{\text{el}} \sigma^4 a_{\text{el}} + \frac{1}{3} \sigma^3 \left(\frac{1}{2} k_{\text{el}} a_{\text{el}}^2 - u_0 \right) \right]. \quad (\text{C3})$$

When $\mathbf{k} \neq 0$, we have

$$\begin{aligned} \tilde{u}_{\text{pseudo}}(\mathbf{k}) &= \int_{-R_{\text{asp}} R_c}^{R_{\text{asp}} R_c} dz \int_0^{\sqrt{R_c^2 - z^2 / R_{\text{asp}}^2}} d\rho \int_0^{2\pi} d\phi \rho \left[\frac{1}{2} k_{\text{el}} (\sqrt{\rho^2 + z^2} - a_{\text{el}})^2 - u_0 \right] e^{-i\mathbf{k}\cdot\mathbf{r}} \\ &\quad - \int_0^\sigma dr \int_0^\pi d\theta \int_0^{2\pi} d\phi r^2 \sin \theta \left[\frac{1}{2} k_{\text{el}} (r - a_{\text{el}})^2 - u_0 \right] e^{-i\mathbf{k}\cdot\mathbf{r}} \\ &= 4\pi \int_0^{R_{\text{asp}} R_c} dz \int_0^{\sqrt{R_c^2 - z^2 / R_{\text{asp}}^2}} d\rho \rho \left[\frac{1}{2} k_{\text{el}} (\sqrt{\rho^2 + z^2} - a_{\text{el}})^2 - u_0 \right] \cos(k_z z) J_0 \left(\rho \sqrt{k_x^2 + k_y^2} \right) \\ &\quad - \frac{2\pi}{k^5} [4k_{\text{el}} k + \{k_{\text{el}}(-4 + 6\sigma)k - k_{\text{el}}(\sigma^3 - 2\sigma^2 + \sigma)k^3 + 2u_0 \sigma k^3\} \cos k\sigma] \\ &\quad + \{-6k_{\text{el}} + k_{\text{el}}(1 - 4\sigma + 3\sigma^2)k^2 - 2u_0 k^2\} \sin k\sigma], \end{aligned} \quad (\text{C4})$$

where J_0 is the Bessel function of the first kind of order zero. We implemented the double integration in the third line using the *Cubature* package.⁹³

We recall our assumption and observation underlying the mapping onto the pseudo-spring system that the interaction does not depend much on the precise location of the boundaries of the Wigner–Seitz cells. This results from the localization of the peaks in the density profiles mainly in the center of the cells.⁴⁹ Therefore, in contrast to the magnetic dipole–dipole interaction, we simply use the same value of $\tilde{u}_{\text{pseudo}}(\mathbf{k})$ obtained for the undeformed geometry also for the deformed systems.

APPENDIX D: IRREDUCIBLE REPRESENTATION FOR STIFFNESS TENSORS

In the framework of linear elasticity theory, irreducible representations for stiffness tensors are determined by the underlying symmetry of the systems. We consider here the strains that are defined in linear elasticity as

$$\epsilon_{ij} \equiv \frac{1}{2} (\nabla_i \mathbf{u}_j + \nabla_j \mathbf{u}_i), \quad (\text{D1})$$

where \mathbf{u} denotes the displacement field. For a tetragonal lattice [(0,0,1)-orientation], the stiffness matrix $\underline{\underline{C}}$ in Mandel

(or orthonormal) notation, where the stiffness matrix becomes a second-rank tensor,^{94,95} takes the form

$$\underline{\underline{C}}_{\text{Mandel}}^{\text{Tetr}} = \begin{pmatrix} \tilde{C}_{00} & \tilde{C}_{01} & \tilde{C}_{02} & 0 & 0 & 0 \\ \tilde{C}_{01} & \tilde{C}_{00} & \tilde{C}_{02} & 0 & 0 & 0 \\ \tilde{C}_{02} & \tilde{C}_{02} & \tilde{C}_{22} & 0 & 0 & 0 \\ 0 & 0 & 0 & \tilde{C}_{33} & 0 & 0 \\ 0 & 0 & 0 & 0 & \tilde{C}_{33} & 0 \\ 0 & 0 & 0 & 0 & 0 & \tilde{C}_{55} \end{pmatrix}. \quad (\text{D2})$$

We note that here the indices run from 0 to 5, not from 1 to 6.

We then turn to nonlinear elasticity. The infinitesimal group generators corresponding to Eq. (D1) are $\{\tilde{\lambda}_i\}$ for $i = 0, \dots, 5$, three of which are defined componentwise via $[\tilde{\lambda}_{i-1}]_{lm} = \delta_{il} \delta_{im}$ for $i, l, m = 1, 2, 3$, and the others by $\tilde{\lambda}_i = \lambda_i$ for $i = 3, 4, 5$. Then we introduce a transformation, which allows us to switch to the generators of Eq. (15). Since a set of infinitesimal group generators is a basis of a vector space, namely, Lie algebra, we can find the form of generalized elastic constants corresponding to Eq. (15) via a linear transformation. Specifically, a unitary transformation

$$\underline{\underline{U}} = \begin{pmatrix} \frac{1}{\sqrt{3}} & \frac{1}{\sqrt{3}} & \frac{1}{\sqrt{3}} & 0 & 0 & 0 \\ \frac{1}{\sqrt{2}} & -\frac{1}{\sqrt{2}} & 0 & 0 & 0 & 0 \\ \frac{1}{\sqrt{6}} & \frac{1}{\sqrt{6}} & -\frac{\sqrt{2}}{\sqrt{3}} & 0 & 0 & 0 \\ 0 & 0 & 0 & 1 & 0 & 0 \\ 0 & 0 & 0 & 0 & 1 & 0 \\ 0 & 0 & 0 & 0 & 0 & 1 \end{pmatrix} \quad (\text{D3})$$

connects, via $\underline{\epsilon} = \underline{\underline{U}} \cdot \underline{\tilde{\epsilon}}$, the deformation vector $\underline{\tilde{\epsilon}} = 1/\sqrt{2}(\tilde{\epsilon}_0, \dots, \tilde{\epsilon}_5)$ in Mandel notation, corresponding to $\{\tilde{\lambda}_i\}$, to $\underline{\epsilon} = (\epsilon_0, \dots, \epsilon_5)$, corresponding to the set of group generators consisting of $\{\lambda_i\}$ for $i = 1, \dots, 5$, and $\lambda_0 \equiv \sqrt{2/3}\mathbf{I}$, where \mathbf{I} is the 3×3 identity matrix, such that $\sum_i \epsilon_i \lambda_i = \sum_i \tilde{\epsilon}_i \tilde{\lambda}_i$. Subsequently, the stiffness tensor $\underline{\underline{C}}_{\text{com}}$ for compressible systems can be computed from $\underline{\underline{C}}_{\text{com}} = \underline{\underline{U}} \cdot \underline{\underline{C}}_{\text{Mandel}} \cdot \underline{\underline{U}}^T$, as is obvious from linear algebra. Within this representation, all deformations involving a volume change are associated with the generator λ_0 . Therefore, under the incompressibility constraint, the components in $\underline{\underline{C}}_{\text{com}}$ associated with λ_0 become irrelevant. Furthermore, predeformations also give rise to additional terms that are

absent in linear elasticity, as demonstrated in Ref. 80. In our case, such nonlinear contributions are all diagonal and associated with the generalized pressure

$$p = -\frac{1}{\sqrt{6}} \frac{\partial \mathcal{F}}{\partial \epsilon_0}, \quad (\text{D4})$$

which only makes sense if a volume change is allowed.

Finally, we conclude that the stiffness tensor of incompressible systems for the tetragonal lattice corresponding to the (0,0,1)-case takes the form of

$$\underline{\underline{C}}_{\text{in}}^{\text{Tetr}} = \begin{pmatrix} C_{11} & 0 & 0 & 0 & 0 \\ 0 & C_{22} & 0 & 0 & 0 \\ 0 & 0 & C_{33} & 0 & 0 \\ 0 & 0 & 0 & C_{33} & 0 \\ 0 & 0 & 0 & 0 & C_{55} \end{pmatrix}, \quad (\text{D5})$$

whose components are defined by Eq. (17).

Second, if the (1,1,1)-direction of the lattice is oriented along the z -axis, we have a rhombohedral lattice (RI Laue group), the stiffness tensor of which, again in Mandel notation, is given as^{96,97}

$$\underline{\underline{C}}_{\text{Mandel}}^{\text{Rhomb}} = \begin{pmatrix} \tilde{C}_{00} & \tilde{C}_{01} & \tilde{C}_{02} & \sqrt{2}\tilde{C}_{03} & 0 & 0 \\ \tilde{C}_{01} & \tilde{C}_{00} & \tilde{C}_{02} & -\sqrt{2}\tilde{C}_{03} & 0 & 0 \\ \tilde{C}_{02} & \tilde{C}_{02} & \tilde{C}_{22} & 0 & 0 & 0 \\ \sqrt{2}\tilde{C}_{03} & -\sqrt{2}\tilde{C}_{03} & 0 & 2\tilde{C}_{33} & 0 & 0 \\ 0 & 0 & 0 & 0 & 2\tilde{C}_{33} & 2\tilde{C}_{03} \\ 0 & 0 & 0 & 0 & 2\tilde{C}_{03} & \tilde{C}_{00} - \tilde{C}_{01} \end{pmatrix}. \quad (\text{D6})$$

Then, the stiffness tensor of the corresponding incompressible systems, within our notation, reads

$$\underline{\underline{C}}_{\text{in}}^{\text{Rhomb}} = \begin{pmatrix} C_{11} & 0 & C_{13} & 0 & 0 \\ 0 & C_{22} & 0 & 0 & 0 \\ C_{13} & 0 & C_{33} & 0 & 0 \\ 0 & 0 & 0 & C_{33} & C_{13} \\ 0 & 0 & 0 & C_{13} & C_{11} \end{pmatrix}. \quad (\text{D7})$$

In summary, the stiffness tensors derived here, i.e., Eqs. (D5) and (D7), are a nonlinear extension of the linear stiffness tensors, e.g., Eq. (D2) for tetragonal lattices, the former of which are now precise up to the second-order of the deformation vector $\underline{\epsilon}$.

REFERENCES

- G. Filipcsei, I. Csetneki, A. Szilágyi, and M. Zrínyi, *Adv. Polym. Sci.* **206**, 137 (2007).
- P. Ilg, *Soft Matter* **9**, 3465 (2013).
- A. M. Menzel, *Phys. Rep.* **554**, 1 (2015).
- S. Odenbach, *Arch. Appl. Mech.* **86**, 269 (2016).
- N. Frickel, R. Messing, and A. M. Schmidt, *J. Mater. Chem.* **21**, 8466 (2011).
- R. Messing, N. Frickel, L. Belkoura, R. Strey, H. Rahn, S. Odenbach, and A. M. Schmidt, *Macromolecules* **44**, 2990 (2011).
- T. Gundermann and S. Odenbach, *Smart Mater. Struct.* **23**, 105013 (2014).
- J. Landers, L. Roeder, S. Salamon, A. M. Schmidt, and H. Wende, *J. Phys. Chem. C* **119**, 20642 (2015).
- L. Roeder, P. Bender, M. Kundt, A. Tschöpe, and A. M. Schmidt, *Phys. Chem. Chem. Phys.* **17**, 1290 (2015).
- J. M. Ginder, S. M. Clark, W. F. Schlotter, and M. E. Nichols, *Int. J. Mod. Phys. B* **16**, 2412 (2002).
- G. Y. Zhou and Z. Y. Jiang, *Smart Mater. Struct.* **13**, 309 (2004).

- ¹²C. Gollwitzer, A. Turanov, M. Krekhova, G. Lattermann, I. Rehberg, and R. Richter, *J. Chem. Phys.* **128**, 164709 (2008).
- ¹³D. Y. Borin, G. V. Stepanov, and S. Odenbach, *J. Phys.: Conf. Ser.* **412**, 012040 (2013).
- ¹⁴E. Y. Kramarenko, A. V. Chertovich, G. V. Stepanov, A. S. Semisalova, L. A. Makarova, N. S. Perov, and A. R. Khokhlov, *Smart Mater. Struct.* **24**, 035002 (2015).
- ¹⁵A. P. Safronov and E. A. Mikhnevich, *J. Phys.: Conf. Ser.* **1389**, 012057 (2019).
- ¹⁶D. Y. Borin, S. Odenbach, and G. V. Stepanov, *J. Magn. Magn. Mater.* **470**, 85 (2019).
- ¹⁷D. V. Saveliev, I. A. Belyaeva, D. V. Chashin, L. Y. Fetisov, D. Romeis, W. Kettl, E. Y. Kramarenko, M. Saphiannikova, G. V. Stepanov, and M. Shamonin, *Materials* **13**, 3297 (2020).
- ¹⁸K. Danas, S. V. Kankanala, and N. Triantafyllidis, *J. Mech. Phys. Solids* **60**, 120 (2012).
- ¹⁹T. Gundermann, P. Cremer, H. Löwen, A. M. Menzel, and S. Odenbach, *Smart Mater. Struct.* **26**, 045012 (2017).
- ²⁰G. Pessot, M. Schümann, T. Gundermann, S. Odenbach, H. Löwen, and A. M. Menzel, *J. Phys.: Condens. Matter* **30**, 125101 (2018).
- ²¹M. Puljiz, S. Huang, K. A. Kalina, J. Nowak, S. Odenbach, M. Kästner, G. K. Auernhammer, and A. M. Menzel, *Soft Matter* **14**, 6809 (2018).
- ²²S. Sturm, M. Sigleitmeier, D. Wolf, K. Vogel, M. Gratz, D. Faivre, A. Lubk, B. Büchner, E. V. Sturm, and H. Cölfen, *Adv. Funct. Mater.* **29**, 1905996 (2019).
- ²³M. Schümann, J. Morich, S. Günther, and S. Odenbach, *J. Magn. Magn. Mater.* **502**, 166537 (2020).
- ²⁴P. Cremer, M. Heinen, A. M. Menzel, and H. Löwen, *J. Phys.: Condens. Matter* **29**, 275102 (2017).
- ²⁵E. Jarkova, H. Pleiner, H.-W. Müller, and H. R. Brand, *Phys. Rev. E* **68**, 041706 (2003).
- ²⁶S. Bohlius, H. R. Brand, and H. Pleiner, *Phys. Rev. E* **70**, 061411 (2004).
- ²⁷T. Potisk, H. Pleiner, and H. R. Brand, *Eur. Phys. J. E* **42**, 35 (2019).
- ²⁸Y. L. Raikher and O. V. Stolbov, *J. Magn. Magn. Mater.* **289**, 62 (2005).
- ²⁹Y. L. Raikher and O. V. Stolbov, *J. Phys.: Condens. Matter* **20**, 204126 (2008).
- ³⁰O. V. Stolbov and Y. L. Raikher, *Arch. Appl. Mech.* **89**, 63 (2019).
- ³¹R. Weeber, S. Kantorovich, and C. Holm, *Soft Matter* **8**, 9923 (2012).
- ³²R. Weeber, S. Kantorovich, and C. Holm, *J. Chem. Phys.* **143**, 154901 (2015).
- ³³E. S. Minina, P. A. Sánchez, C. N. Likos, and S. S. Kantorovich, *J. Magn. Magn. Mater.* **459**, 226 (2018).
- ³⁴O. V. Stolbov, Y. L. Raikher, and M. Balasoiu, *Soft Matter* **7**, 8484 (2011).
- ³⁵D. Ivaneyko, V. Toshchevnikov, M. Saphiannikova, and G. Heinrich, *Condens. Matter Phys.* **15**, 33601 (2012).
- ³⁶L. Fischer and A. M. Menzel, *J. Chem. Phys.* **151**, 114906 (2019).
- ³⁷D. Romeis, V. Toshchevnikov, and M. Saphiannikova, *Soft Matter* **15**, 3552 (2019).
- ³⁸D. S. Wood and P. J. Camp, *Phys. Rev. E* **83**, 011402 (2011).
- ³⁹A. M. Biller, O. V. Stolbov, and Y. L. Raikher, *J. Appl. Phys.* **116**, 114904 (2014).
- ⁴⁰A. M. Biller, O. V. Stolbov, and Y. L. Raikher, *Phys. Rev. E* **92**, 023202 (2015).
- ⁴¹M. Puljiz, S. Huang, G. K. Auernhammer, and A. M. Menzel, *Phys. Rev. Lett.* **117**, 238003 (2016).
- ⁴²M. Puljiz and A. M. Menzel, *Phys. Rev. E* **95**, 053002 (2017).
- ⁴³P. Metsch, K. A. Kalina, C. Spieler, and M. Kästner, *Comput. Mater. Sci.* **124**, 364 (2016).
- ⁴⁴D. Romeis, P. Metsch, M. Kästner, and M. Saphiannikova, *Phys. Rev. E* **95**, 042501 (2017).
- ⁴⁵G. Pessot, P. Cremer, D. Y. Borin, S. Odenbach, H. Löwen, and A. M. Menzel, *J. Chem. Phys.* **141**, 015005 (2014).
- ⁴⁶G. Pessot, H. Löwen, and A. M. Menzel, *J. Chem. Phys.* **145**, 104904 (2016).
- ⁴⁷A. M. Menzel, *Arch. Appl. Mech.* **89**, 17 (2019).
- ⁴⁸A. M. Menzel, *J. Chem. Phys.* **141**, 194907 (2014).
- ⁴⁹S. Goh, R. Wittmann, A. M. Menzel, and H. Löwen, *Phys. Rev. E* **100**, 012605 (2019).
- ⁵⁰R. Evans, *Adv. Phys.* **28**, 143 (1979).
- ⁵¹H. Löwen, *J. Phys.: Condens. Matter* **14**, 11897 (2002).
- ⁵²D. W. Oxtoby, *Annu. Rev. Mater. Res.* **32**, 39 (2002).
- ⁵³R. Evans, M. Oettel, R. Roth, and G. Kahl, *J. Phys.: Condens. Matter* **28**, 240401 (2016).
- ⁵⁴T. Dauxois, S. Ruffo, E. Arimondo, and M. Wilkens, *Dynamics and Thermodynamics of Systems with Long-Range Interactions* (Springer, 2002), pp. 1–19.
- ⁵⁵A. Arnold and C. Holm, “Efficient methods to compute long-range interactions for soft matter systems,” in *Advanced Computer Simulation Approaches for Soft Matter Sciences II*, edited by C. Holm and K. Kremer (Springer, Berlin Heidelberg, 2005), pp. 59–109.
- ⁵⁶M. P. Allen and D. J. Tildesley, *Computer Simulation of Liquids* (Oxford University Press, 2017).
- ⁵⁷S. D. Peroukidis and S. H. L. Klapp, *Soft Matter* **12**, 6841 (2016).
- ⁵⁸N. H. Siboni, G. P. Shrivastav, S. D. Peroukidis, and S. H. L. Klapp, *Phys. Sci. Rev. E* **7**, 1345 (2022).
- ⁵⁹B. Groh and S. Dietrich, *Phys. Rev. Lett.* **72**, 2422 (1994).
- ⁶⁰B. Groh and S. Dietrich, *Phys. Rev. E* **50**, 3814 (1994).
- ⁶¹D. Ivaneyko, V. Toshchevnikov, M. Saphiannikova, and G. Heinrich, *Soft Matter* **10**, 2213 (2014).
- ⁶²P. G. de Gennes, “Weak nematic gels,” in *Liquid Crystals of One-And Two-Dimensional Order* (Springer, 1980), pp. 231–237.
- ⁶³H. R. Brand and H. Pleiner, *Physica A* **208**, 359 (1994).
- ⁶⁴A. M. Menzel, H. Pleiner, and H. R. Brand, *J. Chem. Phys.* **126**, 234901 (2007).
- ⁶⁵A. M. Menzel, H. Pleiner, and H. R. Brand, *Eur. Phys. J. E* **30**, 371 (2009).
- ⁶⁶G. Filippucci and M. Zrinyi, *J. Phys.: Condens. Matter* **22**, 276001 (2010).
- ⁶⁷M. A. Annunziata, A. M. Menzel, and H. Löwen, *J. Chem. Phys.* **138**, 204906 (2013).
- ⁶⁸P. A. Sánchez, O. V. Stolbov, S. S. Kantorovich, and Y. L. Raikher, *Soft Matter* **15**, 7145 (2019).
- ⁶⁹M. V. Vaganov, D. Y. Borin, S. Odenbach, and Y. L. Raikher, *J. Magn. Magn. Mater.* **499**, 166249 (2020).
- ⁷⁰M. Oettel, S. Görig, A. Härtel, H. Löwen, M. Radu, and T. Schilling, *Phys. Rev. E* **82**, 051404 (2010).
- ⁷¹H. Hansen-Goos and R. Roth, *J. Phys.: Condens. Matter* **18**, 8413 (2006).
- ⁷²P. Tarazona, *Phys. Rev. Lett.* **84**, 694 (2000).
- ⁷³R. Roth, *J. Phys.: Condens. Matter* **22**, 063102 (2010).
- ⁷⁴S. H. L. Klapp, *J. Phys.: Condens. Matter* **17**, R525 (2005).
- ⁷⁵T. V. Ramakrishnan and M. Yussouff, *Phys. Rev. B* **19**, 2775 (1979).
- ⁷⁶W. A. Curtin and N. W. Ashcroft, *Phys. Rev. A* **32**, 2909 (1985).
- ⁷⁷A. R. Denton and N. W. Ashcroft, *Phys. Rev. A* **39**, 4701 (1989).
- ⁷⁸Y. Rosenfeld, *Phys. Rev. Lett.* **63**, 980 (1989).
- ⁷⁹R. Ohnesorge, H. Löwen, and H. Wagner, *Europhys. Lett.* **22**, 245 (1993).
- ⁸⁰S. Goh, H. Löwen, and A. M. Menzel, *Phys. Rev. B* **106**, L100101 (2022).
- ⁸¹S. Goh, A. M. Menzel, and H. Löwen, *Phys. Chem. Chem. Phys.* **20**, 15037 (2018).
- ⁸²E. Allahyarov, H. Löwen, and L. Zhu, *Phys. Chem. Chem. Phys.* **17**, 32479 (2015).
- ⁸³G. J. L. Jäger, L. Fischer, T. Lutz, and A. M. Menzel, *J. Phys.: Condens. Matter* **34**, 485101 (2022).
- ⁸⁴N. Queralto Gratacos, “Functional hydrogels: Ferrogel thin films,” Ph.D. thesis, Johannes Gutenberg-Universität Mainz, 2010.
- ⁸⁵S. van Teeffelen, H. Löwen, and C. N. Likos, *J. Phys.: Condens. Matter* **20**, 404217 (2008).
- ⁸⁶L. Fischer and A. M. Menzel, *Smart Mater. Struct.* **30**, 014003 (2020).
- ⁸⁷H. Reich and M. Schmidt, *J. Stat. Phys.* **116**, 1683 (2004).
- ⁸⁸M. Schmidt, *J. Phys.: Condens. Matter* **17**, S3481 (2005).
- ⁸⁹U. M. B. Marconi and P. Tarazona, *J. Chem. Phys.* **110**, 8032 (1999).
- ⁹⁰M. Schmidt and J. M. Brader, *J. Chem. Phys.* **138**, 214101 (2013).
- ⁹¹M. te Vrugt, H. Löwen, and R. Wittkowski, *Adv. Phys.* **69**, 121 (2020).

⁹²Wolfram Research, Inc., Mathematica, Version 11.3, Champaign, IL, 2020.

⁹³S. G. Johnson, Cubature Package, <https://github.com/stevengj/cubature> (accessed 15 October 2022).

⁹⁴M. M. Mehrabadi and S. C. Cowin, *Q. J. Mech. Appl. Math.* **43**, 15 (1990).

⁹⁵M. Maździarz, *2D Mater.* **6**, 048001 (2019).

⁹⁶K. Brugger, *J. Appl. Phys.* **36**, 759 (1965).

⁹⁷J. D. Clayton, *Nonlinear Mechanics of Crystals* (Springer Science & Business Media, 2010), Vol. 177, Chap. [Appendix A](#).